Geologia Croatica
Journal of the Croatian Geological Survey and the Croatian Geological Society
2024 | 77/2 | 159–178 | 18 Figs. | www.geologia-croatica.hr

Tracing the evolution of the world's first mined bauxite from palaeotopography to pyritization: Insights from Minjera deposits, Istria, Croatia

Ivor Perković[1,*], Maja Martinuš[2], Blanka Cvetko Tešović[2], Igor Vlahović[1], Darko Matešić[1], Robert J. Newton[3], Tianchen He[3,4], Marin Šoufek[5], Ivan Razum[5] and Goran Durn[1]

[1] University of Zagreb, Faculty of Mining, Geology and Petroleum Engineering, HR-10000 Zagreb, Croatia;
[2] University of Zagreb, Faculty of Sciences, Department of Geology, HR-10000 Zagreb, Croatia
[3] University of Leeds, School of Earth and Environment, LS2 9JT Leeds, United Kingdom
[4] Hohai University, College of Oceanography, 210024 Nanjing, China
[5] Croatian Natural History Museum, HR-10000, Zagreb, Croatia
(*corresponding author: ivor.perkovic@rgn.unizg.hr)

doi: 10.4154/gc.2024.12

Article history:
Manuscript received: April 16, 2024
Revised manuscript accepted: May 29, 2024
Available online: June 21, 2024

Abstract

The Minjera bauxites are the first analysed and mined bauxites in the world. They are a group of pyritised bauxites situated in northern Istria, developed during the subaerial exposure phase which marked a major part of the Late Cretaceous and Palaeocene in northern Istria. In this study, the morphology, petrography, mineralogy, geochemistry as well as stable sulphur isotopes of the D-1 and D-15 deposits from Minjera were studied, as well as the evolution of their bedrock and cover. This study found that those two deposits differ in morphology, mineralogy and geochemistry as a consequence of their different palaeotopographical positions, with the D-1 deposit located at a higher position at the time of its formation compared to D-15, which led to the higher degree of leaching and desilicification in the D-1 deposit. The pyritisation in the studied deposits was a multi-phase process, which began with the deposition of framboidal pyrite and micrometre-sized anhedral pyrite, over which colloform pyrite was precipitated. This indicates that the solutions were initially supersaturated with iron sulphide, saturation of which subsequently changed, as finally euhedral, dendritic and acicular pyrite were deposited, indicating undersaturated conditions. The final stage was marked by deposition of pyrite veins. This formational sequence of pyrites is also supported by stable sulphur isotopes, as the $\delta^{34}S$ values exhibit a wide range from -40.86 to 2.32 ‰, where lower values indicate an open system with an unrestricted sulphate supply in which supersaturated conditions could have been achieved, while the higher values indicate a change towards a closed system with limited sulphate supply. The organic matter necessary for microbial sulphate reduction was derived from the marshy environment established atop of the bauxite. The initial flooding started in the Palaeocene, with the first part of the sequence being deposited under lacustrine conditions, which changed towards fully marine with the deposition of Foraminiferal limestones.

Keywords: Minjera, Istrian Palaeogene bauxites, Pyritisation in karst bauxites, Iron sulphide morphology in karst bauxites, Stable sulphur isotopes in karst bauxites

1. INTRODUCTION

The Minjera bauxites are a unique and historically important group of karst bauxite deposits from Istria, Croatia, as they represent the first locality where bauxite was mined in the world, even though, at that time, it was not known that this material would be named bauxite in the future. The mining activity dates back as far as the 16th century, but was historically recorded only from 1784 until 1824, when the majority of mining activity occurred (D'AMBROSI, 1926). The bauxite ore was used in the production of alum and vitriol, which were obtained after the ore was processed in the production plant. The ore was particularly suitable for the production of these materials as it has a high pyrite content, a very specific feature of these deposits compared to other Palaeogene bauxites in Istria. All this has made these deposits appealing for geological investigations and field excursions, with the first and most complete study being that by ŠINKOVEC et al. (1994), which was followed by brief investigations for field excursions led by DURN et al. (2003, 2006, 2023).

Pyritised bauxites have been documented all over the Mediterranean bauxite belt (BARDOSSY, 1982; DRAGOVIĆ, 1989; ÖZTÜRK et al., 2002; LASKOU & ECONOMOU-ELIOPOULOS, 2007, 2013; RADUSINOVIĆ & PAPADOPOULOS, 2021, ECONOMOU-ELIOPOULOS et al., 2022), and elsewhere (ZARASVANDI et al., 2012; ELLAHI et al., 2015, 2017; CHEN et al., 2022; ZHAO et al., 2023). The pyritisation phase is a consequence of diagenetic changes and is related to the transgression that followed the bauxitisation phase, during which a marshy environment was established on top of the bauxites, promoting the mobilisation of iron and pyrite formation. Pyrite morphology is a useful tool in the palaeoenvironmental and redox reconstructions in sedimentary settings and in the formation of ore deposits (CHEN, 1978;

RAISWELL, 1982; WIGNALL & NEWTON, 1998; BARRIE et al., 2009; HUANG et al., 2020; HE et al., 2022; MEDERSKI et al., 2022; WANG et al., 2022). This is also used as one of the foundations for the reconstruction of the genetic evolution of pyritised bauxites (ÖZTÜRK et al., 2002; LASKOU & ECONOMOU-ELIOPOULOS, 2007, 2013; ZARASVANDI et al., 2012; ELLAHI et al., 2017; CHEN et al., 2022; ZHAO et al., 2023), which is commonly coupled with the use of stable sulphur isotopes allowing the identification of the sulphur source and its evolutionary pathway which led to pyrite formation (ÖZTÜRK et al., 2002; LASKOU & ECONOMOU-ELIOPOULOS, 2007; CHEN et al., 2022; ZHAO et al., 2023). Such an approach was also used here through careful analysis of iron sulphide morphologies and sulphur isotopes, in an attempt to produce improved reconstruction of diagenetic changes that led to the pyritisation of the Minjera bauxites. Since the flooding of the bauxite and its alteration in a marshy environment is one of the key aspects of those deposits, the Kozina beds from the immediate cover of the bauxites were also studied, in order to better understand the palaeoenvironmental changes that followed the subaerial exposure phase. To additionally enhance the reconstruction of the diagenetic changes that the Minjera bauxite experienced, as well as the original conditions in which they formed, the trace and rare earth elements (REE) were carefully studied. Namely, their behaviour has been extensively used to reconstruct the genesis of different bauxite deposits, since they respond to physico-chemical changes, intensity of chemical weathering as well as changes in pH and redox potential (MAKSIMOVIĆ et al., 1991; MAKSIMOVIĆ & PANTÓ, 1991; MONGELLI, 1997; ABEDINI & CALAGARI, 2014; MONGELLI et al., 2014, 2017; ELLAHI et al., 2017; ABEDINI et al., 2018, 2019; YANG et al., 2019; TOMAŠIĆ et al., 2021).

Overall, this study aims to enhance the current knowledge regarding the historically important Minjera bauxites and Istrian Palaeogene bauxites in general, through the construction of an updated genetic model based on different analytical methods, which should also prove useful in the future studies of pyritised bauxites elsewhere.

2. REGIONAL GEOTECTONIC SETTING

Palaeogene bauxites are common throughout northern, eastern and southern Istria, and their stratigraphic position fits within the widespread Perimediterranean bauxitization event resulting in formation of a vast bauxite belt stretching from Hungary through Slovenia, Croatia, Bosnia and Herzegovina, Montenegro, and Albania to Greece.

This widespread bauxitization event coincided with the Late Cretaceous closure of the Vardar Ocean (SCHMID et al., 2008, 2020; van HINSBERGEN et al., 2020), which led to the formation of a large foreland basin in the area of today's Internal Dinarides, causing the tectonic uplift of the Adriatic Carbonate Platform area due to the development of the flexural forebulge in response to the overburden pressure generated by the advancing nappes (OTONIČAR 2006, JEŽ & OTONIČAR, 2018). The emerged areas in the flexural forebulge served as the environment in which the Palaeogene bauxites of Istria and Dalmatia formed. Consequently, these bauxites belong to those formed in collisional settings, known as type-1 bauxites according to D'ARGENIO & MINDSZENTY (1995).

The duration of subaerial exposure between the Cretaceous and Palaeogene in Istria lasted mostly between 28 My (in southern Istria and Mt. Učka klippe) and 40 My (in northern Istria). However, in the Western Istrian Anticline subaerial exposure locally persisted for more than 75 My, as indicated by erosional remnants of Eocene Foraminiferal limestones which locally transgressively cover different levels of karstified Lower Cretaceous limestones (the oldest being Valanginian in age; MATIČEC et al., 1996). More than 10,000 bauxite occurrences and small bauxite deposits are known in Istria (Milan Mihovilović, pers. comm.), serving as evidence of widespread and intense bauxitization during this period. As deformation continued, rapid subsidence of the foreland area along the partially exposed former Adriatic Carbonate Platform commenced, leading to restoration of marine carbonate production in the form of Foraminiferal limestones, followed by deepening, recorded by transitional marls and turbidites (VLAHOVIĆ et al., 2005).

3. GEOLOGICAL SETTING

The Minjera bauxites are located in the easternmost part of the northern Istrian Buzet–Savudrija Anticline (Fig. 1), also known as the Buje Anticline (BERGANT et al., 2020). Bauxites are situated on karstified Upper Cenomanian limestones belonging to the Milna Fm. (BERGANT et al., 2020), with their hanging wall comprising the freshwater to brackish Palaeogene Kozina beds (ŠINKOVEC et al., 1994).

During the Albian, relatively uniform shallow-marine environments predominated over the entire area of the Adriatic Carbonate Platform. However, in northern Istria, significant changes in depositional environments occurred during the early Cenomanian (VLAHOVIĆ et al., 1994). In the western part of northern Istria, shallow marine sedimentary environments persisted, while in the central part, prograding sand bars composed of finely crushed rudist and chondrodont bioclasts formed. In contrast, the eastern part of northern Istria, including the study area, experienced a deepening of sedimentary environments. There, in addition to typical lagoonal limestones, hummocky cross-stratified deposits occasionally occurred in the offshore-transition zone, along with limestones reflecting pelagic influences containing calcisphaeres, silicisponge spicules, algae, and rare planktonic foraminifera (VLAHOVIĆ et al., 1994). Towards the end of the Cenomanian, a gradual regression occurred throughout northern Istria, leading to a regional unconformity in the area, although pelagic influences persisted occasionally in the eastern part.

Throughout the entire area of the Savudrija–Buzet Anticline, the topmost parts of the Upper Cenomanian limestones are heavily karstified due to subaerial exposure. In the studied area of the Mirna River valley, an irregularly karstified surface is covered with numerous small bauxite bodies and transgressive Palaeogene beds. Intense karstification occurred especially along fractured zones, resulting in numerous smaller and larger sinkholes and decametre-sized karstic canyons that served as sediment traps for the accumulation of the source material for bauxite formation. The red colour and common oolitic structure of the Palaeogene

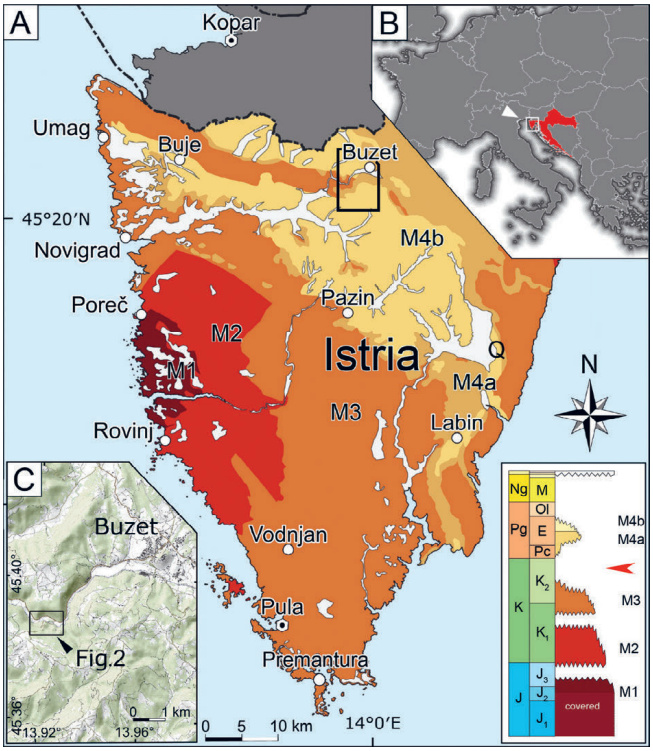

Figure 1. Geological map of the Istrian peninsula and its position in Europe. A – Geological map of Istria, modified after VELIĆ et al. (1995) with the schematic geological column. Legend: M1 – 1st Megasequence (lower Bathonian–lower Kimmeridgian); M2 – 2nd Megasequence (upper Tithonian–lower/upper Aptian); M3 – 3rd Megasequence (lower/upper Albian–upper Santonian); M4a – Carbonate deposits of the 4th Megasequence (mostly lower–middle Eocene); M4b – Clastic deposits of the 4th Megasequence (middle–upper Eocene); Q – Quaternary deposits. Position of the Palaeogene bauxites on the schematic geological column is indicated by a red arrow. (B) Map of central, western and southern Europe with the indicated location of Istrian peninsula. (C) Map of Buzet area and geographic position of the Minjera bauxites.

bauxites in northern Istria indicate highly elevated and intensely karstified carbonate bedrock, typical of vadose lithofacies in carbonate terrains uplifted at least several dozen metres above sea level (D'ARGENIO & MINDSZENTY, 1995). Some bauxite occurrences in northern Istria were exposed to reduced pore waters during the subsequent transgression, resulting in the reduction of iron oxides and the precipitation of iron sulphides. In some cases entire bauxite bodies were exposed to this process, resulting in their complete transformation into grey and pyritised bauxite, as observed in the Minjera bauxites. The transgression was marked by deposition of the Palaeogene Kozina beds directly overlying the bauxites, deposited in freshwater and brackish ponds developed in a network of bauxite-filled sinkholes, empty palaeodepressions, and vadose canyons. The Kozina beds in this area consist of a sequence of bituminous, gastropod-rich limestones with some coal seams. The presence of charophyte oogonia in most layers confirms a freshwater to brackish-water depositional environment, although their alternation with layers abundant in milliolids indicates periodic marine incursions during their deposition (ŠINKOVEC et al., 1994). The Kozina beds are overlain by Foraminiferal limestones, indicating a gradual transition to open marine environments on the slopes of the newly formed Pazin foreland basin to the south.

4. MATERIALS AND METHODS

After detailed investigation of all deposits from the Minjera locality, only two deposits (D-1 and D-15; Fig. 2) were deemed suitable for further investigation, since they still contained enough unweathered bauxite. These two deposits were selected for sampling, with the addition of the red bauxite sample from the tailing heaps left by the historic mining activity, which was found next to the D-14 deposit (Fig. 2). In the D-15 deposit most bauxite samples were collected from the sides of the deposit, as most of the bauxite was completely mined out. Two smaller profiles (Profile 1 – Fig. 2A: D15-1, D15-2, D15-3 and D15-10, Profile 2 – Fig. 2B: D15-5, D15-6, D15-7 and D15-8) encompassing the upper metre of the bauxite were sampled, as well as a portion close to the bedrock (D15-4), and the top section of the bauxite in the adit (D15-9). In the D-15 deposit, the footwall and the hanging wall of the bauxite were sampled over a total thickness of 6.1 m (Figs. 4, 6C). In the D-1 deposit, samples were collected in the lower section of the deposit, as the upper section was not accessible. Most of the samples were collected on the eastern side of the deposit (D1-1 to D1-9, Fig. 6), while additional samples were collected from the central part of the deposit (D1-10 to D1-12; Fig 6D). In this deposit, only the bedrock of the deposit was sampled. Red bauxite was collected from tailing heaps near one of the historic processing plants (Fig. 2), as it was previously located in the centre of the pyritised deposits but it was mined out from all deposits (ŠINKOVEC et al., 1994).

Thin-sections were prepared from all the limestone and bauxite samples. Additionally, thin-sections were made from separated heavy and light mineral fractions using sodium polytungstate (SPT) solution (3.0 g/cm^3) after obtaining granulometric fractions ranging from 250 to 63 μm from both the grey and the red bauxite. Prior to sieving, iron oxides from the red bauxite underwent dissolution using the Dithionite-Citrate-Bicarbonate method (MEHRA & JACKSON, 1960) to release individual mineral grains. All thin sections were

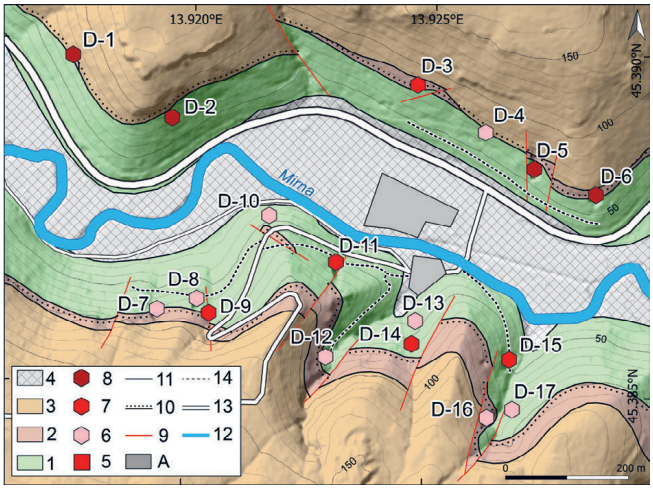

Figure 2. Geological map of the Minjera area with different types of bauxite deposits indicated, modified after ŠINKOVEC et al (1994). Legend: 1 – Upper Cenomanian limestones; 2 – Palaeocene Kozina beds; 3 – Eocene Foraminiferal limestones; 4 – Quaternary; 5 – Red bauxite tailing heaps; 6 – Sinkhole bauxite deposits; 7 – Small canyon bauxite deposits; 8 – Large canyon bauxite deposits; A – Remnants of the processing plants and infrastructure from the past mining activities.

analysed using the OPTIKA B-1000 series polarizing microscope, equipped with the OPTIKA C-P6 FL camera and OPTIKA PROVIEW software. Bauxites were analysed following the micromorphological and petrographic methodologies outlined by BARDOSSY (1982), while sedimentological and micropalaeontological analyses of limestone sections were performed according to FLÜGEL (2004). For the additional study of iron sulphide morphology and general mineralogy SEM-EDS was employed on three samples, using the TESCAN VEGA GMU SEM. EDS analysis was also used, and was available using live SEM scanning window of Essence™ software using a fully integrated energy dispersive X-ray spectroscopy (EDS) detector.

X-ray powder diffraction (XRPD) analysis was conducted on most bauxite samples. A portion of each sample was gently crushed and sieved through a 0.5 mm sieve. Subsequently, samples were milled in a McCrone micronizing mill for 15 minutes with a mixture of 2 ml of the sieved material and 7 ml of isopropyl alcohol. The resulting slurry was air-dried and disaggregated in an agate pestle and mortar. Dried samples were side-loaded to ensure random orientation and uniform grain size, essential for accurate Rietveld refinement. Rietveld refinement was performed using Profex version 5.2.4 software (DOEBELIN & KLEEBERG, 2015), utilizing structural data from built-in files and the crystallography open database (GRAULIS et al., 2009).

To determine concentrations of major, minor, trace, and rare earth elements, five bauxite samples from both deposits and one red bauxite sample were selected. These samples were analysed using inductively-coupled-plasma mass-spectrometry (ICP-MS) at the Bureau Veritas, Canada commercial laboratory. Analysis was performed using the lithium metaborate/tetraborate fusion and nitric acid digestion. Total sulphur and carbon values were measured separately from other major oxides. Trace element and rare earth element (REE) values were normalized to the upper continental crust values according to TAYLOR & MCLENNAN (1985).

Samples from both deposits were selected for stable sulphur isotope analysis. The procedure started with silver sulphide extraction from pyrite in the samples using the chromous chloride distillation method (CANFIELD et al., 1986). Sulphur-isotope analysis was undertaken on the resulting silver sulphide precipitates, which was performed on an Elementar vario PYRO cube linked to a GV Isoprime mass spectrometer in continuous flow mode, in the Cohen Geochemistry Laboratories of the School of Earth and Environment, University of Leeds. About 0.150 mg of silver sulphide was weighed and packed into tin cups, which was afterwards flash-combusted at 1150 °C in the presence of pure research grade O_2 and helium carrier gas to produce SO_2. Excess O_2 was consumed by reaction with copper wires at 850 °C and water was removed by a Sicapent trap. Subsequently, SO_2 was separated from other gases using a temperature-controlled trap and purge column. Results were calibrated to the Vienna-Canyon Diablo Troilite (V-CDT) using a seawater laboratory standard (SWS-3) and a chalcopyrite inter-lab standard (CP1), with their respective values of +20.3 and -4.56 ‰, respectively. The calibration of this material was in turn performed using the IAEA S-3 (-32.06 ‰) international standard.

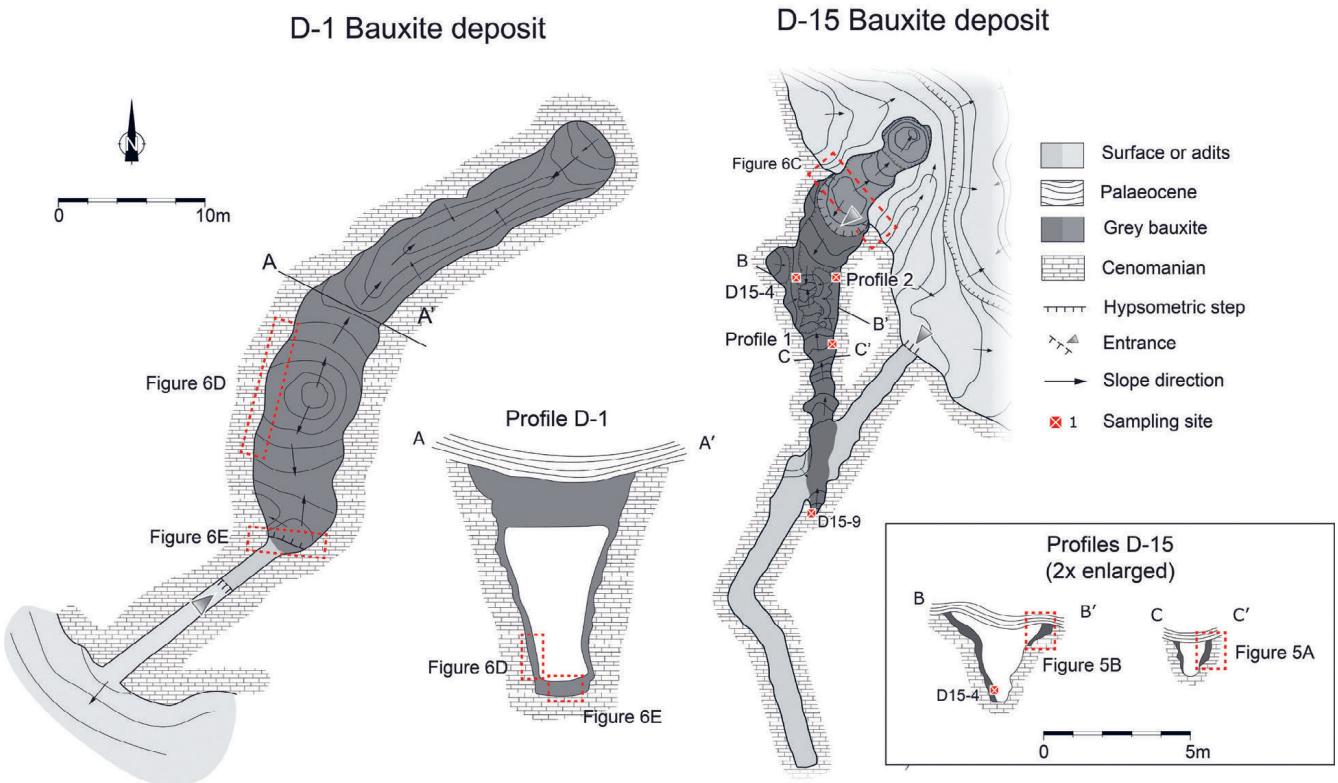

Figure 3. Plans of the D-1 and D-15 deposits with their respective cross-sections and sampling sites. Note that the B–B' and C–C' cross-sections are enlarged with respect to both plans and A–A' cross-section, in order to demonstrate the sampled profiles and sample positions more clearly.

5. RESULTS

5.1. Outcrop and field descriptions

5.1.1. Bauxite bedrock and cover – lithostratigraphy and biostratigraphy

The Minjera section comprises the 3.6 m thick succession of Upper Cenomanian beds underlying the regional unconformity and the D-15 Bauxite deposit, and the 3.4 m thick Palaeogene beds overlying the bauxite (Fig. 4). Based on the macro- and microscopic lithological and microfossil features, four lithofacies types (LF1–LF4) were differentiated (Fig. 4). Peloidal-bio-intraclastic wackestone–packstone to packstone–grainstone with small benthic foraminifera, fragmented and micritized bivalve shells and in places small pelagic bioclasts

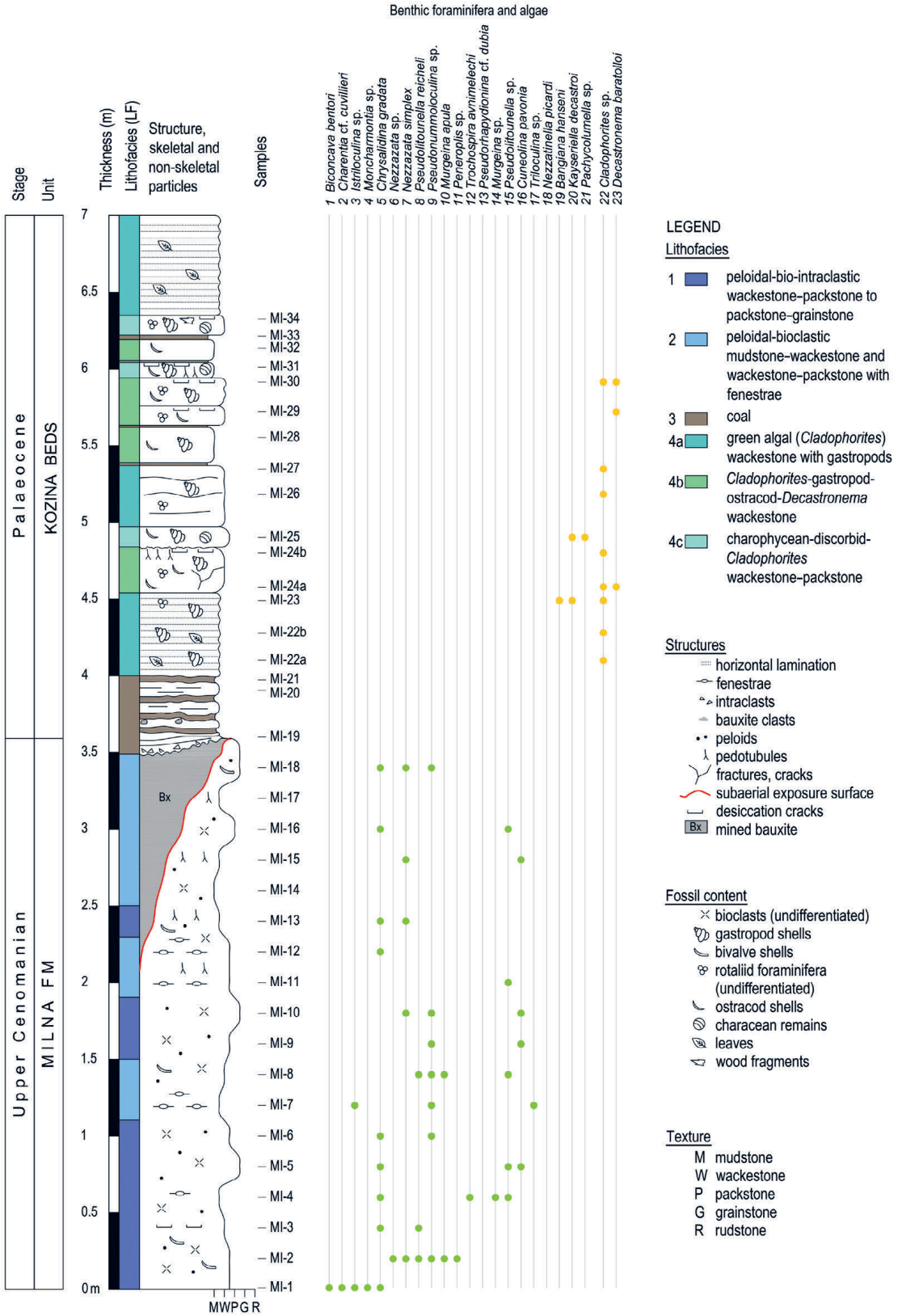

Figure 4. A stratigraphic column of the Minjera section (D-15 Bauxite bedrock and cover) with structures, fossil content, lithofacies and biostratigraphy.

(LF1), in the lower part of the Cenomanian strata indicate formation in subtidal environments of an inner carbonate platform, with occasional input of material from the open sea (Fig. 5A, B). The upper part of the Cenomanian strata comprises peloidal-bioclastic mudstone–wackestone and wackestone–packstone with similar fossil content (LF2), but the presence of fenestrae, circumgranular cracks and pedotubules indicates shallowing of the depositional environment (very shallow subtidal and intertidal) and occasional subaerial exposures preceding the prolonged terrestrial phase marked by the regional unconformity (Fig. 5C–E). A microfossil assemblage composed of various benthic foraminifera, among which the most important taxa are *Chrysalidina gradata*, *Nezzazata simplex*, *Pseudolituolunella reicheli*, *Trochospira avnimelechi*, *Pseudonummuloculina* sp., and *Cuneolina pavonia*, indicates the upper Cenomanian age of the strata underlying the regional unconformity at the studied Minjera locality (Fig. 4).

The irregular unconformity and the D-15 Bauxite deposit is overlain by decimetre-thick beds of brownish to dark grey lacustrine limestones (LF4; Figs. 4, 6C), which include centimetre- to decimetre-thick coal interbeds in their base, formed in freshwater marsh (LF3; Fig. 5F). The contact between the bauxite and the cover sequence is marked by dark brown, organic matter- and coal-rich bauxite mixed with large carbonate pebbles and in places boulders likely eroded from the surrounding carbonate rocks and embedded within the top sections of the bauxites during the initial flooding of the area. In their lower part, the lacustrine limestones are composed of green algal (*Cladophorites*) wackestone with gastropod shells and rare small rotalids indicating lacustrine near-shore and shore depositional settings (LF4a; Fig. 5G, H). The middle part is composed of wackestone with *Cladophorites*, gastropod shells, *Decastronema*, ostracods, and discorbids commonly with pedotubules and in places desiccation cracks, indicating a lake shore environment with plants (LF4b; Fig. 5I). In the

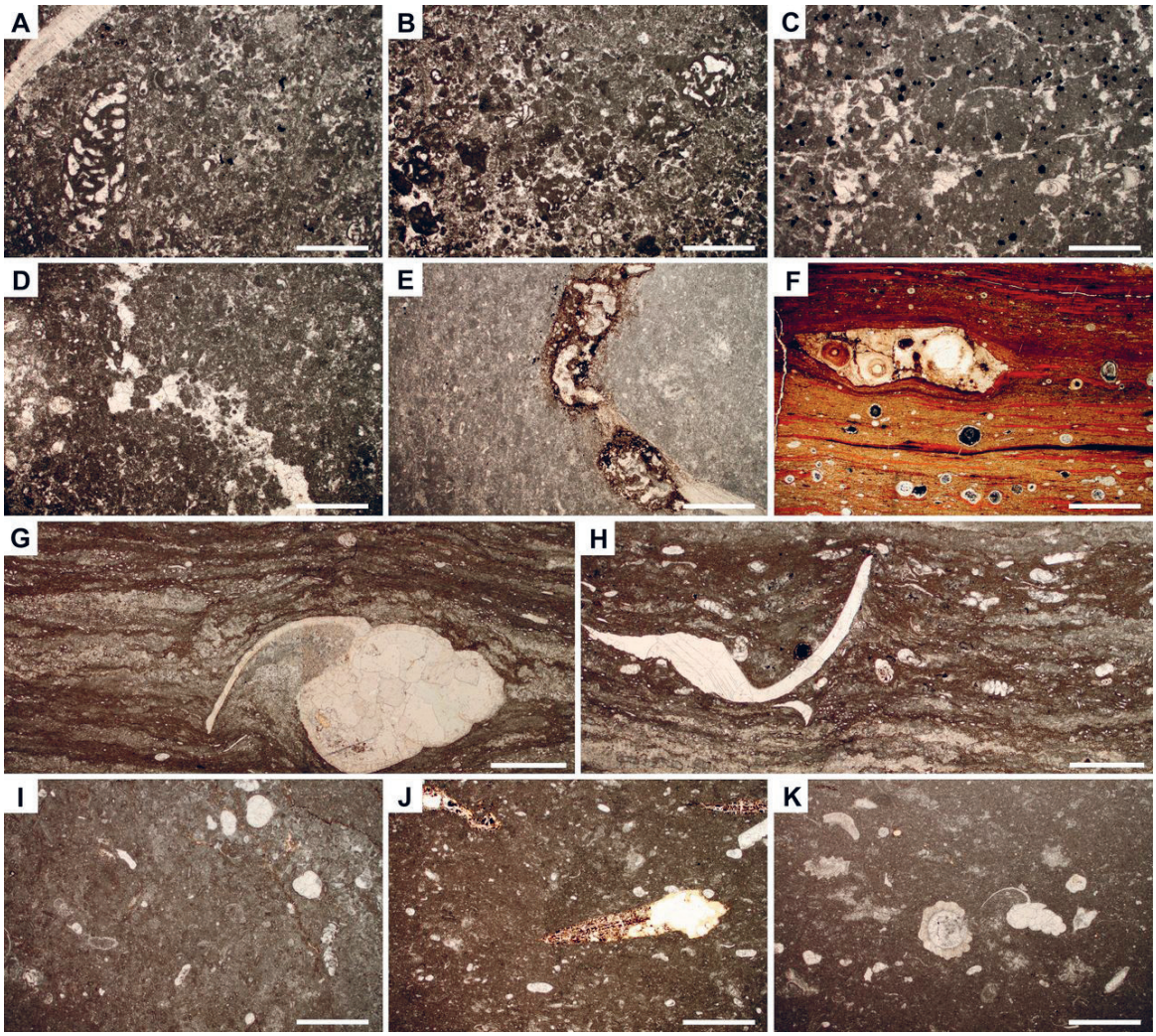

Figure 5. Photomicrographs of the lithofacies (LF) in the Minjera bauxite bedrock and cover. A – LF1: Peloidal packstone-grainstone with benthic foraminifera (sample MI-6). B – LF1: Peloidal-bio-intraclastic packstone-grainstone (sample MI-10). C – LF2: Bioclastic mudstone with circumgranular cracks and rare benthic foraminifera (sample MI-8). D – LF2: Fenestral peloidal mudstone-wackestone with rare benthic foraminifera (sample MI-16). E – LF2: Indistinctly laminated peloidal-bioclastic wackestone with pedotubules (sample MI-17). F – LF3: Laminated coal with iron ooids (pisoids) (sample MI-20). G – LF4a: Laminated green algal (*Cladophorites*) mudstone-wackestone (bafflestone) with gastropod shells (sample MI-22a). H – LF4a: Laminated green algal (*Cladophorites*) mudstone-wackestone with gastropod shells and rotalid foraminifera (sample MI-23). I – LF4b: *Decastronema*-ostracod-discorbid wackestone (sample MI-24a). J – LF4c: Discorbid-charophycean wackestone (sample MI-34). K – LF4c: Discorbid-charophycean wackestone with wood fragments (sample MI-34). Size of the scale bar is 1 mm on all photomicrographs.

upper part of the lacustrine limestones, charophycean-discorbid wackestone prevails with discorbids, charophycean oogonia and thalli parts, *Cladophorites*, gastropod and ostracod shells, and in places wood fragments (LF4c; Fig. 5J, K). Such fossil remains indicate similar lacustrine near-shore settings including brackish environments of a coastal lake. Small rotalid foraminifera often present in thin laminae in all lithofacies were probably transported by storm events from neighbouring marine environments. The microfossil assemblage including *Bangiana hanseni, Kayseriella decastroi* and fragments of *Pachycolumella* indicates a Palaeocene age of the strata directly overlying the D-15 Bauxite deposit at the studied Minjera locality (Fig. 4).

5.1.2. Description of bauxite deposits

Three main deposit types were distinguished based on field observations (Fig. 2): the large canyon (elongated, deeper than 10 metres and between 20 and 40 metres in its longer axis), small canyon (elongated, less than 10 metres deep with the longer axis shorter than 20 metres) and sinkhole deposits (spherical, less than 10 metres deep and smaller than 10 metres in diameter). Most of the smaller canyon and sinkhole deposits are located south of the Mirna River, while most of the large canyon deposits are located north of the Mirna River. The D-1 deposit is of the large canyon type, being very steep, almost 40 metres long and thicker than 15 metres (Figs. 2 and 3), while the D-15 deposit represents the smaller canyon type, as it is less steep, up to 20 metres long and up to five metres thick (Figs. 2 and 3). The bauxite from these two deposits also differs macroscopically, with those from the D-15 being mostly grey (Fig. 6A and B) and those from the D-1 deposit being darker due to the higher pyrite content (Fig. 6D and F). Coal-rich bauxite can be found on top of the bauxite in both D-1 (Fig. 6A and B) and D-15 deposits, but it has only been sampled in the D-15 deposit. In the D-15 and other deposits, it can be seen that a number of carbonate clasts are embedded within the bauxite in its uppermost part (Fig. 6A and B). Several pyritised bauxite types can be discerned visually: the "striped" or "spotted" bauxite composed of a grey matrix within which large veins or spots of iron sulphides are visible (Fig. 6G), grey bauxite containing visibly very little pyrite (Fig. 6A, B, D, F), and black bauxite completely impregnated with iron sulphides (Fig. 6D and F). Pyritised root relics have also been observed but only in the grey bauxite from the D-15 deposit.

5.2. Petrography and micromorphology

All bauxite samples from D-1 and D-15 deposits as well as sampled red bauxite have oolitic texture (Fig. 7A–F), with varying proportions of ooids (sensu BARDOSSY, 1982) and the pelitomorphic matrix. The ooids in the red bauxite are between 50 and 200 μm in size, composed of iron oxide-rich and oxide-poor laminae, with the majority having an iron oxide-poor outer cortex (Fig. 7A). Large bauxite clasts can also be found in the red bauxite (Fig. 7A), which are usually richer in iron oxides than the surrounding matrix, but occasionally have a deferrified outer rim. The aforementioned iron oxide enrichment and depletion in clasts and ooids was preserved through pyritisation in samples from both the D-1 and D-15 deposits, as the pyritised ooids display an alternation of pyrite-rich and pyrite-poor laminae (Fig. 7B), while bauxite clasts commonly contain more iron sulphides than the surrounding matrix (Fig. 7C). In places, in the D-15 deposit, the ooids are

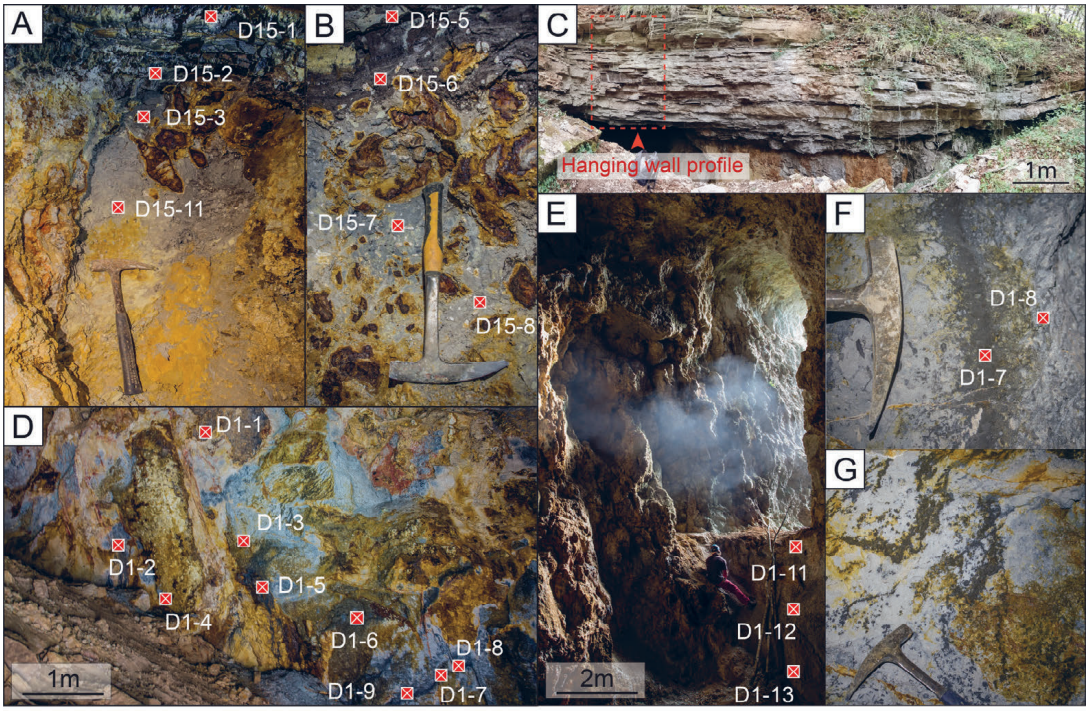

Figure 6. Photographs of the sampled profiles and sample positions. A – Profile 1 in the D-15 deposit with sample locations, composed of grey and coal-rich bauxite; B – Profile 2 in D-15 deposit with sample locations, composed of grey and coal-rich bauxite; C – Bauxite hanging wall composed of Kozina limestones in the D-15 deposit, with indicated position of the sampled hanging wall; D – Profile 1 in the D-1 deposit with indicated sample positions; E – entrance into the adit exposing D-1 deposit with indicated sample positions on the second profile; F – zonation of pyrite-poor and pyrite-rich bauxite with indicated sample positions; G – "striped" and "spotty" bauxite, composed of pyrite-poor bauxite and veins or spots of pyrite-rich bauxite.

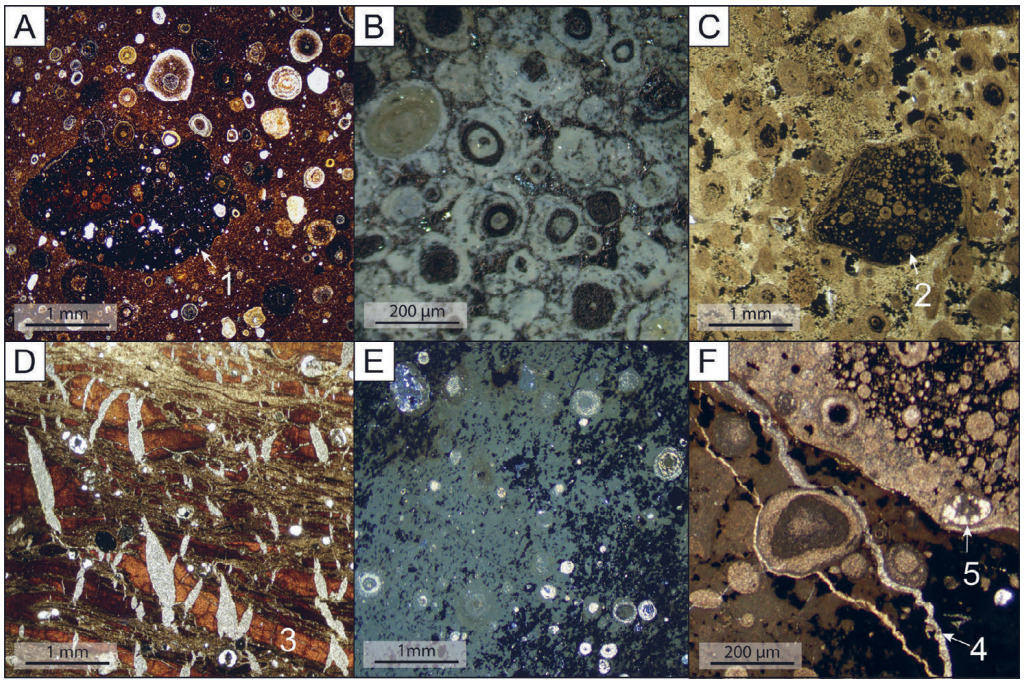

Figure 7. Photomicrographs of red, pyritised and coal-rich bauxite in plane-polarised (PPL)B or cross-polarised light (XPL). A – red bauxite with numerous ooids with visible deferrification in their cortices or lamellae, and a clast of iron-oxide rich oolitic bauxite (1), sample RB (PPL); B – kaolinitised and pyritised ooids, sample D1-3 (XPL); C – pyritised oolitic bauxite with a completely pyritised bauxite clast (2), sample D15-9 (PPL); D – coal-rich bauxite, composed of fan-like alternation of coal intercalations (3), reworked bauxite material and ooids, with the coal lenses cross-cut by gypsum veins, sample D1-6 (PPL); E – Pyritised bauxite with visible ooids composed of boehmite, sample D1-3 (XPL); , F – Pyritised bauxite clast and diaspore veins (4) and nests (5), sample D15-9 (PPL).

completely replaced by kaolinite (Fig. 7B). Organic matter and coal were also detected, but only in the coal-rich bauxite, alternating with reworked bauxite clasts and ooids (Fig. 7D). The samples from the D-15 deposit contain less aluminium oxide minerals than those from the D-15 deposit. The aluminium oxide minerals are diaspore and boehmite in both deposits. These two minerals make up the iron-poor laminae in ooids (Fig. 7E) and they are also likely present in the cryptocrystalline matrix. Besides the ooids, diaspore is also present in veins or nests (Fig. 7F). The two deposits also differ in their iron sulphide content, the D-1 deposit contains much more iron sulphide, while the D-15 deposit contains less iron sulphide. The iron sulphides are mainly present as pyrite in both deposits with the sporadic occurrence of marcasite. Pyrite displays an array of different morphologies, most of which are present in both deposits. It is present as framboids with a diverse size range between 5 and 40 µm, which are either present individually in the matrix (Fig. 8A), or are aggregated (Fig. 8C) and concentrated within the pores between ooids or in the matrix. Framboids are commonly associated with micrometre-sized anhedral pyrite (MSAP, Fig. 8B), which also impregnates large portions of the bauxite matrix in some samples (Figs. 4C and D), as well as ooid lamellae and bauxite clasts (Fig. 8D). Both the framboids and MSAP are frequently overgrown with colloform pyrite, which is present as: 1 – impregnations of MSAP (Fig. 8D), 2 – thin overgrowths of individual framboids (Fig. 8A), and 3 – large-scale impregnations, overgrowths and replacements of MSAP and framboids in the matrix (Fig. 8C), ooid laminae (Fig. 8D) or bauxite clasts. Colloform pyrite also forms banded textures in places and is commonly overgrown with euhedral pyrite (Fig. 8F). Euhedral pyrite can be also found as a replacement of individual framboids within the matrix (Fig. 8E), preserving their original size and shape, dominated by octahedrons and hexahedrons (Fig. 8E). Dendritic pyrite was also observed, mainly present as overgrowths over euhedral pyrite (Fig. 8G). Acicular pyrite also formed in some samples and is exclusively present in the bauxite matrix (Fig.8H). The pyrite veins were found in most samples, cross-cutting other pyrite features and structural elements (Fig. 8I and J). Pyritised root remains were found in the samples from the D-15 deposit, composed of hollow tubes of colloform or euhedral pyrite, filled with matrix material or some authigenic phase such as diaspore or kaolinite (Fig. 8L). Besides pyrite, marcasite was also found, but mostly in rosettes composed of elongated crystals smaller than 100 µm (Fig. 8K).

Extracted light and heavy mineral fractions were also studied: in the heavy mineral fraction staurolite, grunerite-cummingtonite, tourmaline and barite were detected (Figs. 9A–D), while chert and opal were detected in the light mineral fraction (Figs. 9E and F). Most of the minerals from the heavy mineral fraction and chert are rounded to subrounded, while only barite displays some euhedral grains. Opal is found as irregular masses and shards, indicating its authigenic origin.

5.3. XRPD

The mineralogical composition was primarily analysed using XRPD, as most phases in bauxites are hard to identify microscopically due to their cryptocrystalline occurrence. Clear differences in mineralogy were found between the D-1 and D-15 deposits, with the samples from the D-1 deposit containing much higher amounts of pyrite and boehmite

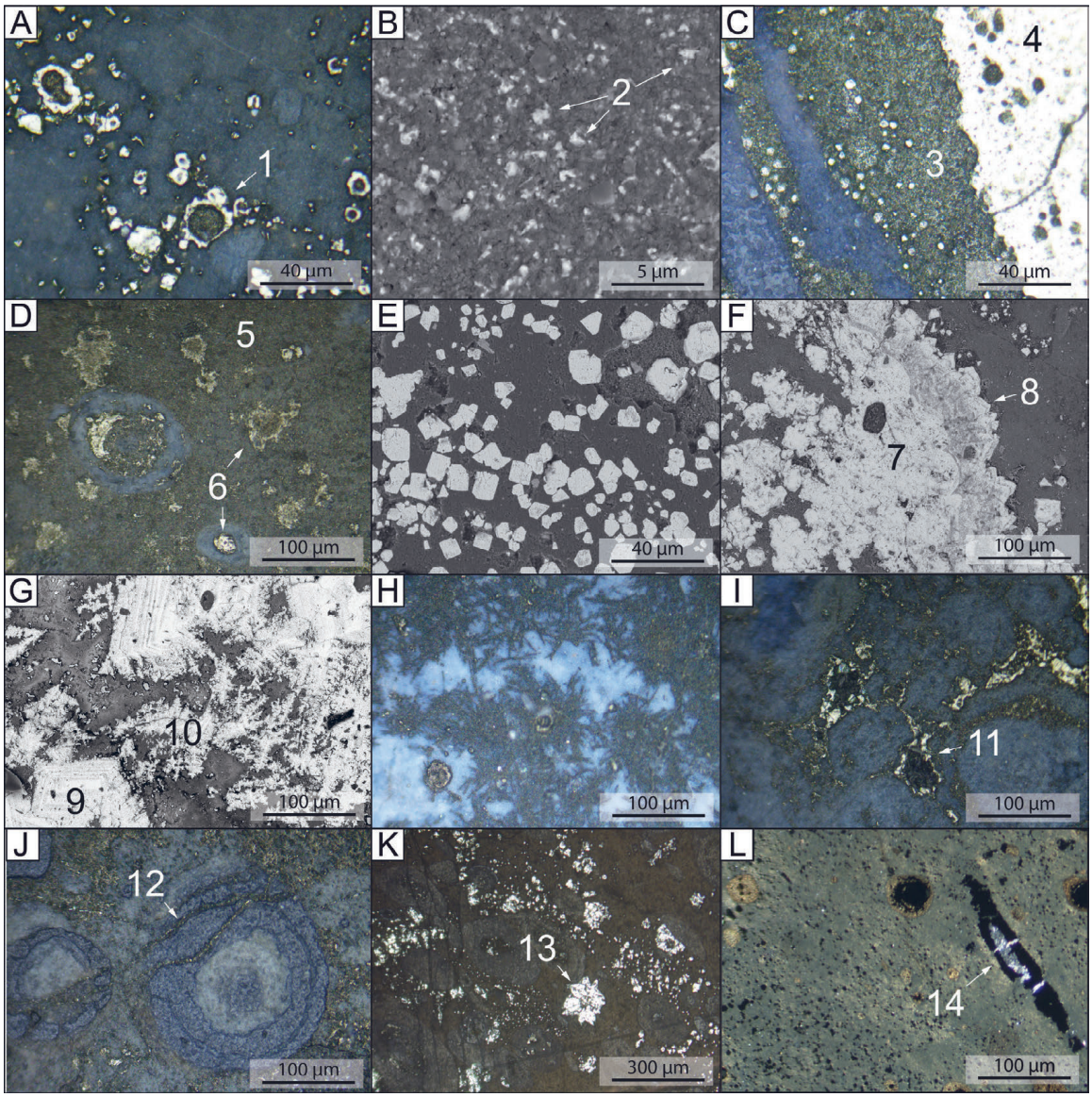

Figure 8. Photomicrographs taken using XPL or reflected light (RL) and BSE images of different iron sulphide morphologies. A – Pyrite framboids (1) overgrown with colloform pyrite, sample D15-10 (RL); B – dispersed grains of MSAP (2) in the bauxite matrix, sample D15-10 (BSE); C – Mixture of pyrite framboids and MSAP (3) overgrown with colloform pyrite (4), sample D1-12 (RL); D – photomicrograph of pyritised ooids and bauxite matrix impregnated with MSAP (5), with visible impregnations of colloform pyrite (5) and replacement of MSAP with colloform pyrite in ooid lamellae (6), sample D1-3 (RL); E – individual euhedral pyrite crystals in the bauxite matrix, sample D1-3 (BSE); F – colloform pyrite (7) overgrown with euhedral pyrite crystals with visible growth bands (8), sample D15-10 (BSE); G – euhedral pyrite crystals (9) overgrown with dendritic pyrite (10), sample D15-10 (BSE); H – acicular pyrite crystals in the bauxite matrix, sample D1-6 (RL); I – veins composed from pyrite and kaolinite (11), sample D1-8 (RL); J – Ooid cross-cut by pyrite veins (12), sample D1-9 (RL); K – marcasite rossete (K) in bauxitic matrix with different pyrite morphologies, sample D15-10 (RL); L – pyritised root filled with diaspore crystals (14), sample D15-8 (XPL).

compared to samples from the D-15 deposit, which mostly have a lower boehmite content and higher kaolinite content (Fig 10). Based on this, samples from the D-1 deposit are genuinely bauxites while the ones from D-15 deposit are clayey bauxites. In both deposits, variable amounts of diaspore and marcasite are present, together with anatase, rutile and different secondary sulphate minerals such as pickeringite, jarosite and gypsum. Red bauxite differs from those samples since it is composed mainly of boehmite and haematite with smaller amounts of kaolinite, anatase and rutile.

5.4. Geochemistry and stable sulphur isotopes

The major oxide content of the studied samples is in accordance with their mineralogical composition, with the pyrite- and boehmite-rich samples from the D-1 deposit having a higher amount of Fe_2O_3, LOI, Na_2O and TOT/S, while the kaolinite-rich samples from the D-15 deposit have higher amounts of CaO, K_2O, MgO, MnO and SiO_2 (Fig. 11). The D15-6 sample is an exception in the D-15 deposit, as it has a lower content of the aforementioned elements and is enriched in TOT/C (Fig. 11), indicating its high organic matter content, which corresponds to the abundance of coal in that sample (Fig. 7D). Compared to samples from both the D-1 and D-15 deposits, red bauxite has a higher Cr_2O_3 and MnO and lower LOI, Na_2O, P_2O_5 and TOT/S values (Fig. 11). The ternary diagram SiO_2–Al_2O_3–Fe_2O_3 (after ALEVA, 1994) also highlights the differences between the two deposits (Fig. 12), as most of the samples from the D-15 deposit are kaolinitic bauxites or pure

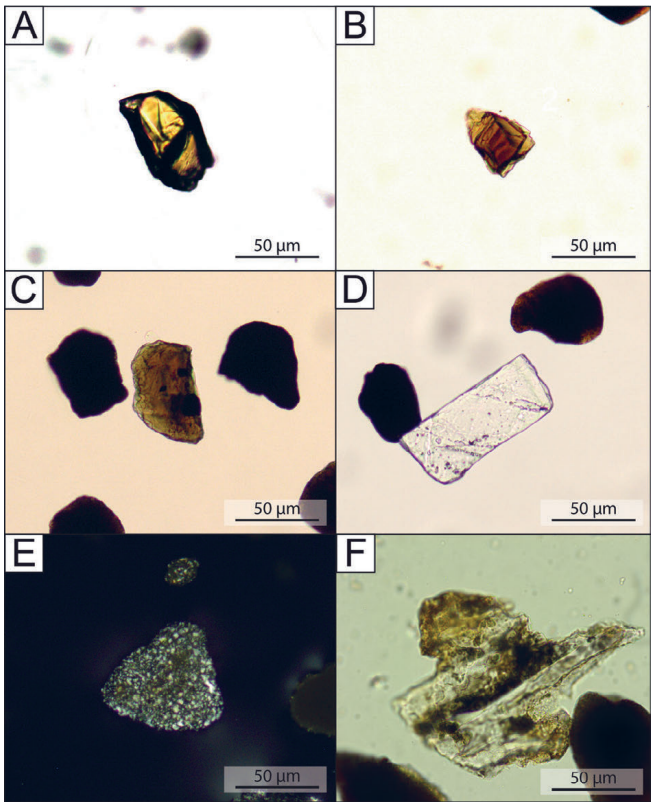

Figure 9. Photomicrographs of different mineral grains from the light and heavy mineral fractions in PPL. A – staurolite, B – cummingtonite-grunerite group amphibole, C – tourmaline, D – baryte, E – chert, F – opal.

bauxites, while those from the D-1 deposit are ferritic bauxites or pure bauxites. The red bauxite falls in the ferritic bauxite field.

The differences between the deposits and sample types are also visible in the trace element contents. The samples from the D-1 deposit are enriched in As, Cu, Co, Ni and Sb when compared to the D-15 deposit and red bauxite, while the samples from the D-15 deposit are enriched in Ba, Cs, Rb, Sr, U and Zn compared to D-1 deposit and red bauxite (Fig. 13). Samples from both deposits are enriched in Cd, Hg, Mo, Se and Tl, as well as depleted in Bi, Ga, Nb, Sn, Ta, Th, V and Zr compared to the red bauxite sample (Fig. 13). Red bauxite has a higher Ga, Nb, Pb, Sn, Ta, Th, V and Zr content than samples from D-1 and D-15 deposits (Fig. 13). While showing some similarities to other samples from the D-15 deposit, the coal-rich bauxite shows several differences – higher Hg, Mo and Sb values and lower values of Co, Cs, Cu, Ni, Pb, Th and Tl (Fig. 13). Compared to the upper continental crust, all samples are enriched in As, Ga, Hf, Hg, Nb, Ni, Sb, Sn, U, V, W, Y and Zr, while being depleted in Ba, Rb, Se and Sr (Fig. 14A).

Rare earth elements display similar trends in all sample types with few variations. Generally, all samples display a "saddle" pattern, with a visible depletion in middle rare earth elements (MREE) compared to Light (LREE) and heavy rare earth elements (HREE, Fig. 14B–D). Red bauxite has a higher HREE and MREE content than the samples from the D-1 and D-15 deposits, and a pronounced negative Ce anomaly (Fig. 15). Samples from the D-1 and D-15 have the same REE patterns (Fig. 14B, C), but the samples from D-15 deposit have higher LREE values, total REE values and La/Y ratios, as well as lower Y/Ho ratios (Figs. 14B, C and 15). The D15-6 differs from the rest of the samples from the D-15 deposit in REEs as well, having lower LREE values and La/Y as well as higher Y/Ho values (Figs. 14C and 15). Both deposits display either very low negative Ce anomalies or their absence (Fig. 15).

$\delta^{34}S$ values do not display any apparent differences between the deposits and their position within them (Fig. 16). Their values range between -40.86 to 2.32 ‰ (Fig. 16).

6. DISCUSSION

6.1. Genesis of the Minjera deposits

The Minjera bauxites were developed over the karstified upper Cenomanian limestones which announced the subaerial exposure phase, partly through the shallowing of the depositional environment and the repeated occurrence of brief subaerial exposure surfaces and partly by features such as fenestrae, circumgranular cracks and pedotubules. Finally, the start of the subaerial exposure phase is indicated by the formation of the Minjera bauxites in the studied area. The source and the type of material from which the Minjera

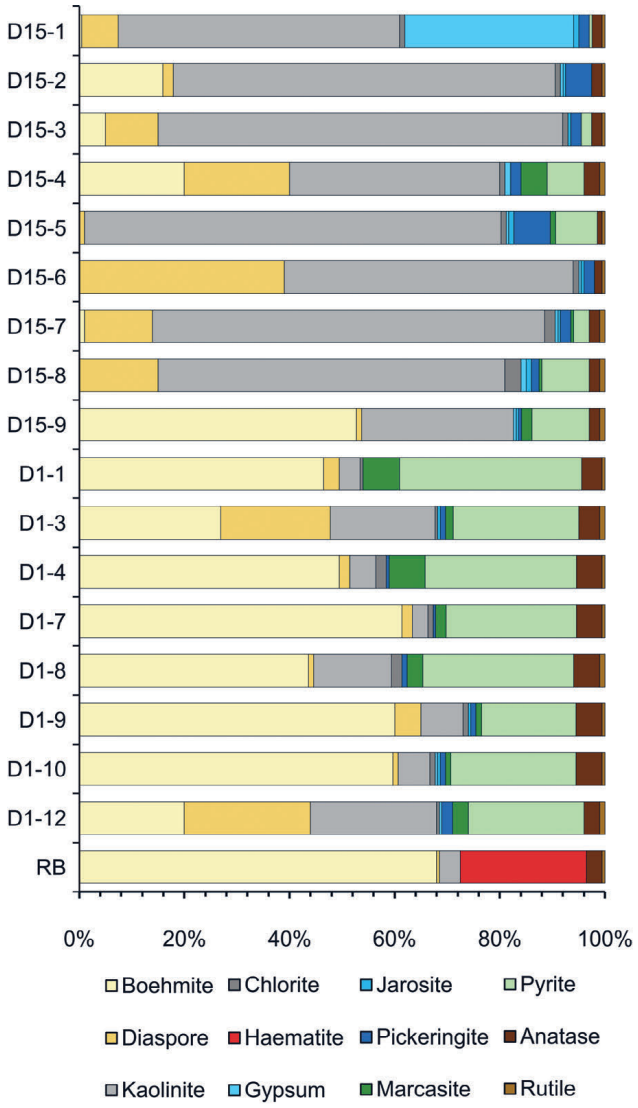

Figure 10. Mineralogical bulk composition of samples analysed using XRPD.

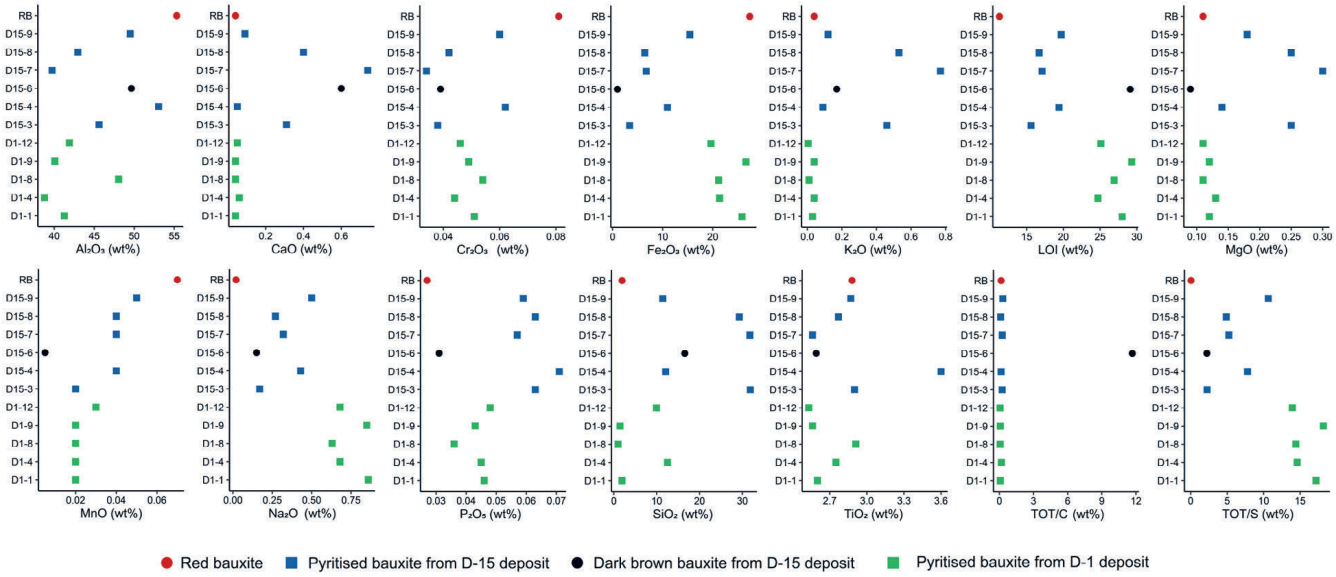

Figure 11. Values of different major oxides plotted against individual samples.

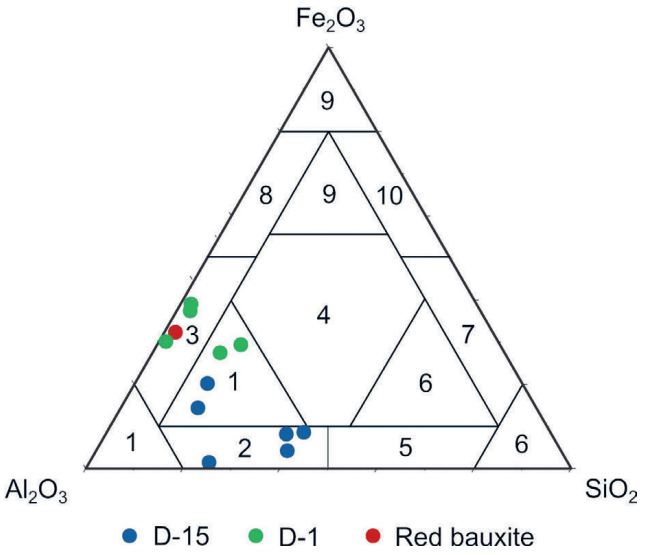

Figure 12. A bauxite classification diagram based on Al_2O_3 Fe_2O_3 and SiO_2 content according to ALEVA (1994). 1 – bauxite, 2 – kaolinitic bauxite, 3 – ferritic bauxite, 4 – laterite, 5 – bauxitic kaolinite, 6 – kaolinite, 7 – ferritic kaolinite, 8 – bauxitic ferrite, 9 – ferrite, 10 – kaolinitic ferrite, 11 – ferrite.

bauxites have formed is hard to determine, since bauxitisation leads to the loss of primary textures, structure and composition of the parent material. Nevertheless, the material from which these bauxites formed can be tentatively reconstructed based on the content of the light and heavy mineral fractions. The presence of metamorphic minerals such as staurolite, tourmaline and clinohumite-grunerite amphiboles (Fig. 5A–D) indicate the contribution of a mixture of aeolian material during its formation. The insoluble residue from the underlying carbonates can neither be confirmed nor disputed and should be regarded as a possible minor source of the parent material. Karst bauxites are also commonly formed from volcanic dust (BARDOSSY, 1982; D'ARGENIO & MINDSZENTY, 1995; KELEMEN et al., 2017, 2023; BRLEK et al., 2021), but there is no evidence for such an input in the case of the Minjera bauxites, as no zircons have been found which could have been dated and connected to contemporaneous volcanic activity. The deposition and accumulation of source materials for the bauxites was initiated by the tectonic deformation of the Adriatic Carbonate Platform in response to the load of the advancing nappes following the closure of the Vardar Ocean at the end of the Cretaceous (VAN HINSBERGEN et al., 2020; SCHMID et al., 2008, 2020). Following this, karstification also ensued, creating a diverse karst landscape, as seen by the different morphologies and sizes of the Minjera deposits (Fig. 2). The prevalence of large canyon deposits north of the Mirna River and their absence south of the river coupled with the abundance of sinkhole and smaller canyon deposits (Fig. 2) suggests the geomorphological differences between these two areas. The Kozina beds are also much thicker south of the Mirna River (Fig. 2), indicating altogether the lower palaeotopographical position of the deposits on the southern side compared to the northern side, which resulted in the formation of deeper karstic features on the northern side. This is reflected in the mineralogical and geochemical composition of the two studied bauxite deposits, as the differences in the morphology of the deposits affected the drainage and the intensity of fluid-flow of percolating porewaters. The larger and steeper D-1 deposit has a higher boehmite content compared to the D-15 deposit, and is composed of bauxite and ferritic bauxite (Fig. 12). The D-15 deposit contains more kaolinite (Fig. 10) and is composed of bauxite and kaolinitic bauxite (Fig. 12), which is probably a result of better drainage and higher distance from the water table in the D-1 deposit and vice-versa. The clear relationship between bauxites and their palaeotopographical position was described by D'ARGENIO & MINDSZENTY (1995) and has also been observed in other studies (YANG et al., 2017; MO et al., 2023), indicating that the bauxite lithofacies and grade depend on their position in the karst terrains. Based on this, the bauxites on the northern side of the Mirna River can be attributed to the vadose bauxite lithofacies, while those from the southern side represent the intermediate bauxite lithofacies sensu D'ARGENIO & MINDSZENTY (1995). Diagenetic resilicification is a

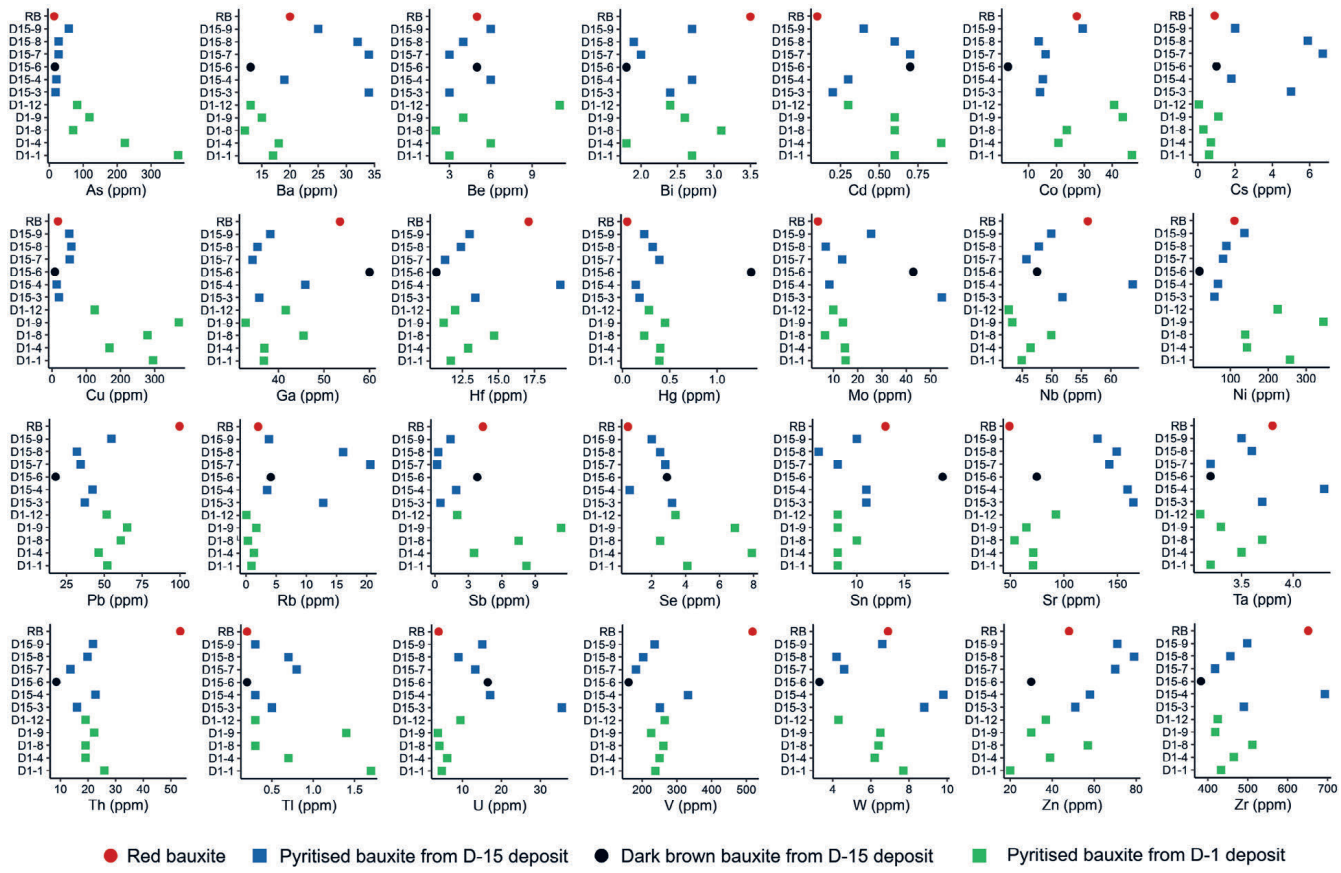

Figure 13. Values of different trace elements plotted against individual samples.

common phenomenon in bauxites after their formation (BARDOSSY, 1982; MAMELI et al., 2007; MONGELLI et al., 2021) and should not be excluded as a factor resulting in the higher kaolinite content of the D-15 deposit, as the replacement of boehmite with kaolinite in ooids can be seen in some samples (Fig. 7B). Veins filled by an association of pyrite and kaolinite crystals were also found (Fig. 8I) in both deposits, indicating that resilicification was also present in the D-1 deposit. Diaspore also formed during this phase, replacing boehmite in the bauxite matrix and within the ooids but also forming nests within the pyritised roots and the bauxite as well as in veins (Figs. 7F and 8L). Diaspore can form in several ways, either in response to increasing pressure during burial diagenesis (BARDOSSY, 1982; WILLIAMS, 2014; GAMALETSOS et al., 2017; MONDILLO et al., 2022), or it can form in the reducing environment (NIA, 1968; BARDOSSY, 1982; D'ARGENIO & MINDSZENTY, 1995; LIU et al., 2013; ZHANG et al., 2022). In the case of Minjera bauxites, it is clear that diaspore formation happened in reducing conditions, as it crystallised directly from percolating solutions, as indicated by its presence in nests and veins (Figs. 7F and 8L). A proportion of diaspore might also be inherited from the originally red bauxite, as a minor amount of diaspore has been detected in the red bauxite (Fig. 10).

6.2. Iron sulphide morphology and stable sulphur isotopes

A large number of iron sulphide morphologies were found in the Minjera bauxites, the formation of which was initiated as the microbial sulphate reduction and dissolution of iron oxides

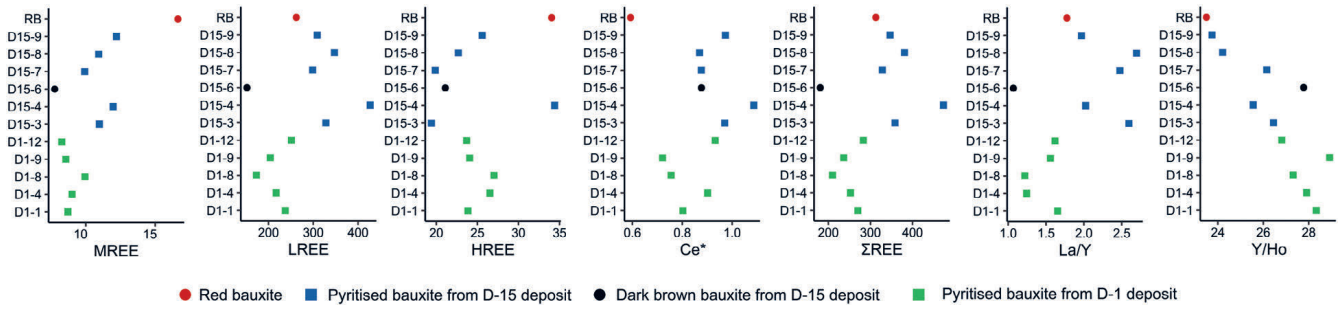

Figure 14. Values of trace elements and rare elements in different samples after normalisation against the upper continental crust. A – values of trace elements, B – values of rare earth elements in the D-1 deposit, C – values of rare earth elements in the D-15 deposit, D – values of rare earth elements in the red bauxite.

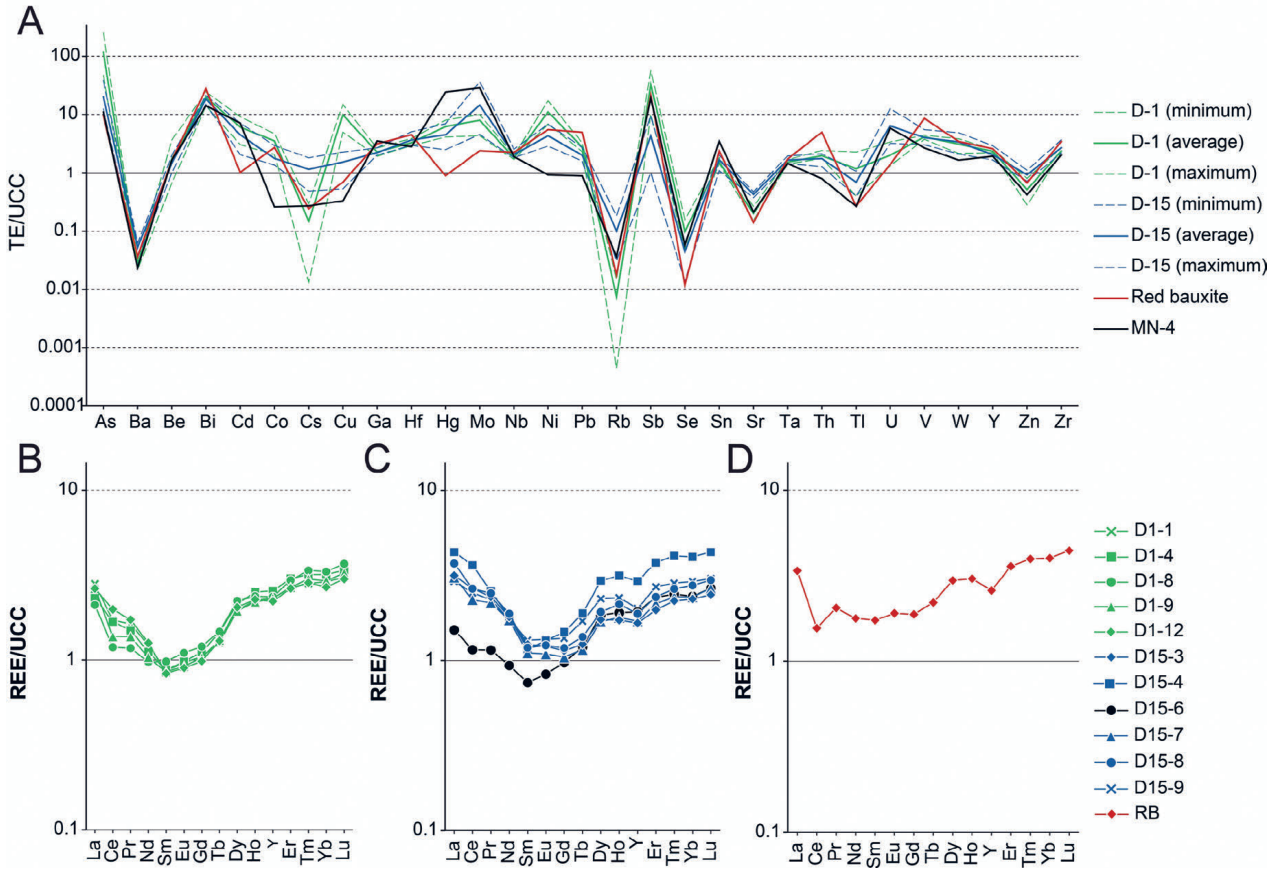

Figure 15. Values of different REE groups, total REE content, Ce anomaly and different REE ratios plotted against individual samples.

began in a newly established marshy environment. Macroscopically, they exhibit several different types across the two studied deposits, where they form bands and nodules within the iron-poor bauxite matrix in the cases of "striped" and "spotted" pyritised bauxites (Fig. 6G). This can be linked to the differences in the redox potential and the degree of pyrite saturation in the porewaters, allowing its crystallisation in spots or bands, with the bands of the "striped" bauxite being controlled by the direction of fluid-flow. In the case of the D-1 deposit, a zonal arrangement of pyrite-rich and pyrite-poor bauxite was observed, with the increase of pyrite content towards the interior of the deposit, with the completely pyritised region separating the zone with less and more pyrite (Fig. 6F). This zonation is parallel to the karstified bedrock and is probably a result of changes in the redox potential, with the completely pyritised zone likely indicating the redox boundary, where conditions for iron sulphide precipitation were apparently optimal. This could also reflect the pH differences within the sediment, as the inflow of saline and karstic porewaters during the flooding of the bauxite was the highest in this zone, where the pyrite-rich zone could reflect the zone with near-neutral to slightly alkaline conditions which are generally required for its formation (WILKIN & BARNES, 1996). On the micro-scale, there is a clear order in the formation of different iron sulphide morphologies (Figs. 17 and 18). The first pyrite morphologies that formed (Figs. 17 and 18) were the framboidal pyrite and the impregnations of MSAP (Figs. 8A–D), which formed in the pore spaces, in the matrix (Figs. 8B, 8D and 18A), as a replacement of roots (Figs. 8L and 18A), or as an in-situ replacement of originally iron oxide-rich bauxite clasts and ooid lamellae (Figs. 7B, 7C and 18A). It should be noted that pyrite framboids were also found in other pyritised bauxites (LASKOU & ECONOMOU-ELIOPOULOS, 2007; ZARASVANDI et al., 2012; ECONOMOU-ELIOPOULOS et al., 2022), appearing to be a common feature in pyritised bauxites. Framboidal pyrite usually forms first from the initially precipitated iron monosulphides (BERNER, 1970; HÁMOR 1994), which can then serve as crystallisation sites for later stages of pyrite growth (YUE et al., 2020). As such, both the framboids and MSAP were overgrown by colloform pyrite (Figs. 8A, C and D). The presence of both framboidal and colloform pyrite in the first two stages (Figs. 17, 18A and 18B) indicates that the solutions were supersaturated with respect to pyrite (ROEDDER, 1968; CHEN, 1978; BARRIE et al., 2009). It should be noted that the colloform pyrite also frequently displays a banded character, indicating the fluctuations in pyrite saturation during its precipitation (BARRIE et al., 2009). The formation of colloform pyrite was followed by the formation of euhedral pyrite which overgrows framboids as well as colloform pyrite (Figs. 8F and 18C), and which replaces framboids with individual euhedral crystals (Figs. 8E and 18C). The formation of euhedral pyrite indicates that the porewaters became undersaturated with respect to pyrite in this stage (RAISWELL, 1982; BARRIE et al., 2009; CAVALAZZI et al., 2012; HE et al., 2022). They also commonly display distinct growth bands, where some of them contain matrix impurities (Fig. 8F), indicating the fluctuations in growth rates. The further drop in pyrite saturation is

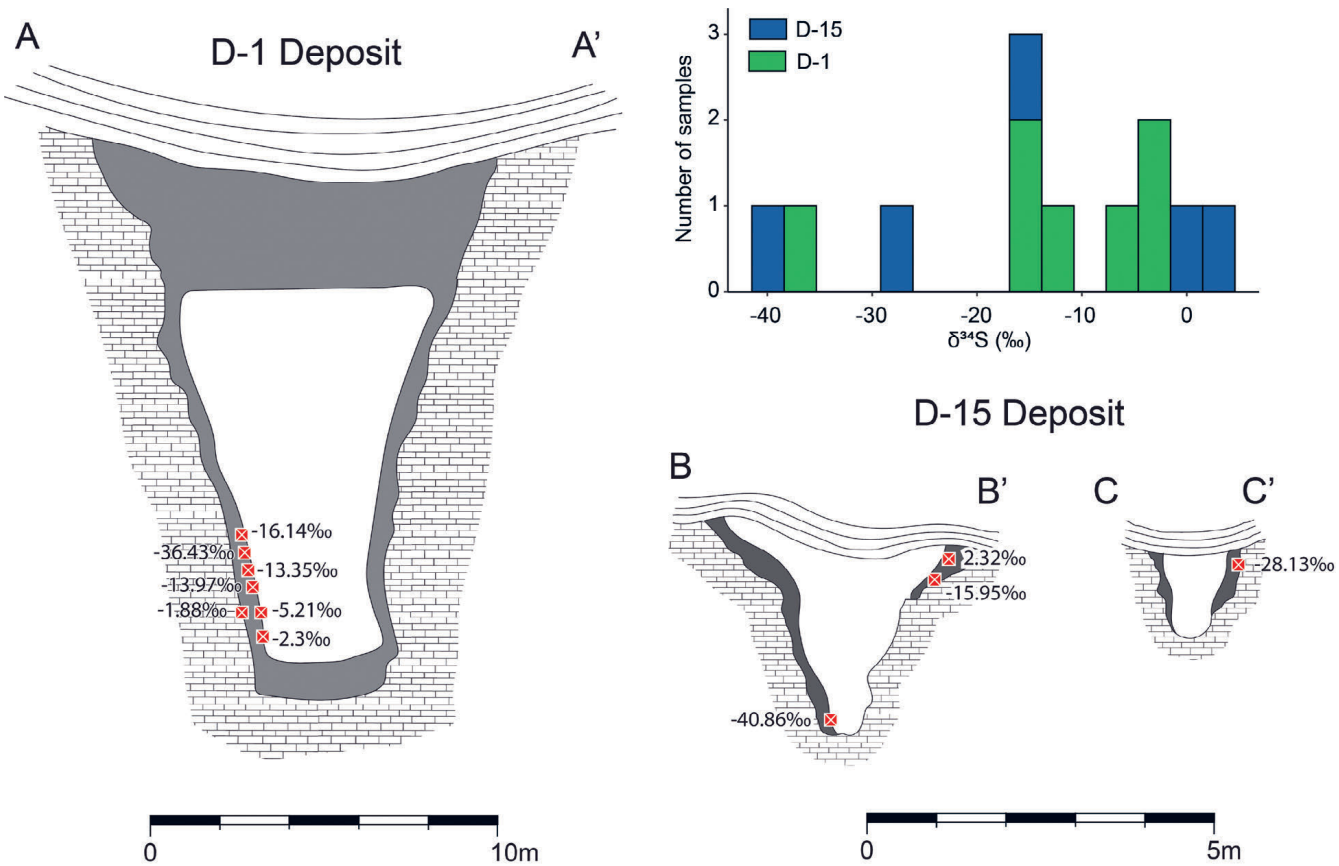

Figure 16. The position of different $\delta^{34}S$ values in the D-1 and D-15 deposits, together with the histogram of obtained $\delta^{34}S$ values.

recorded via the precipitation of dendritic pyrite (BARRIE et al., 2009), which represents the final overgrowth on the previously deposited pyrite morphologies where present (Figs. 8G and 18C). Its formation is also coupled with the crystallisation of acicular pyrite (Figs. 8H, 17 and 18C). The final pyrite deposition and late diagenesis is marked by the consolidation and brittle fracturing of the bauxite within which the final stage of iron sulphides precipitated as pyrite and kaolinite veins (Figs. 8K, 8L, 17 and 18D). Marcasite is found only as rosettes or radial crystal clusters which cannot be precisely related to any of the stages of pyrite formation (Figs. 8K and 17). Its presence indicates the local presence of acidic conditions within the deposit, as La/Y ratios >1 indicate that the bauxites generally formed under alkaline to near-alkaline conditions (Fig. 11; MAKSIMOVIĆ & PANTÓ, 1991). Stable sulphur isotope values indicate the role of microbial sulphate reduction in pyrite formation, as most of the $\delta^{34}S$ values are negative (Fig. 16). Similar $\delta^{34}S$ values were

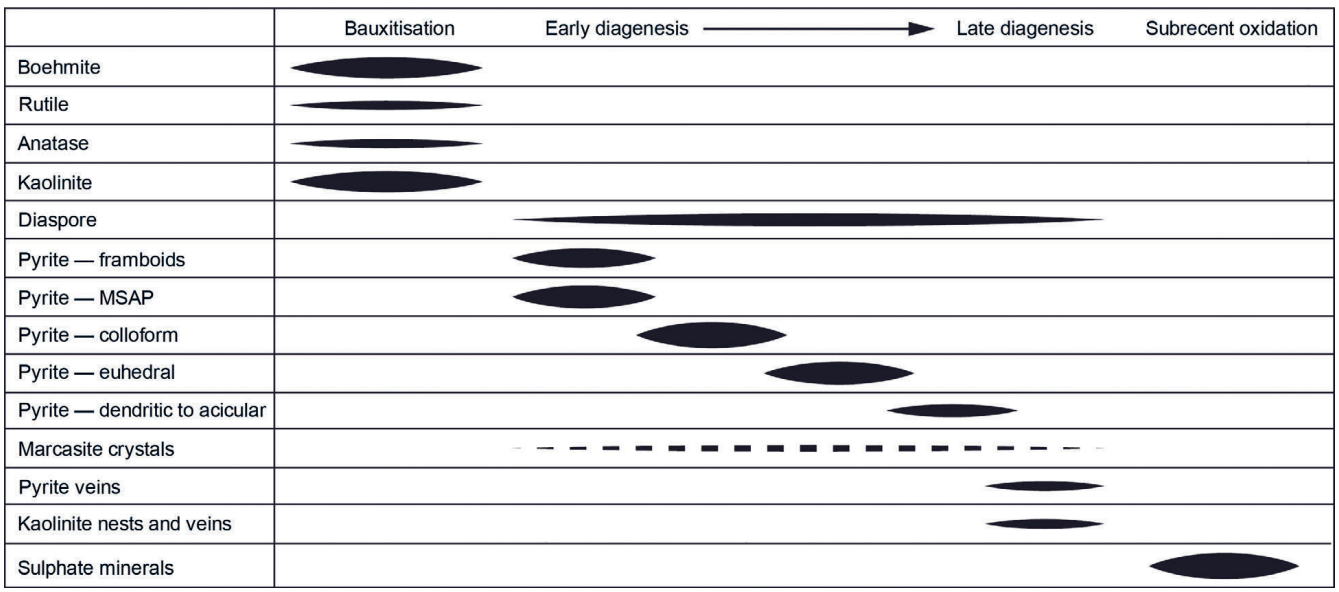

Figure 17. A paragenetic sequence of the Minjera deposits and the succession of the formation of different iron sulphide morphologies.

found in most pyritised bauxites where stable sulphur isotopes were studied (ÖZTÜRK et al., 2002; LASKOU & ECONOMOU-ELIOPOULOS, 2007; ZARASVANDI et al., 2012; ELLAHI et al., 2015; ZHAO et al., 2023). The $\delta^{34}S$ values from the Minjera bauxite also display a wide range of values, from -40.86 to 2.32 ‰ (Fig. 16), which compared to the global seawater ^{34}S values between 17 ‰ and 19 ‰ during the Late Cretaceous and Palaeocene (ALGEO et al., 2015) yield enrichment factors between -60 ‰ and -15 ‰. The high negative values indicate that the system was open, since the sulphate content was not limited, allowing the continuous enrichment of ^{32}S via microbial reduction (CHAMBERS & TRUDINGER, 1979; ALGEO et al., 2015; PASQUIER et al., 2017; HOUGH et al., 2019). The sulphate-rich marine to brackish solutions were likely pumped through the underground karstic conduits and channels through tidal pumping, a common phenomenon which induces salinity changes in blue holes in the Bahamas (MARTIN et al., 2012; SMITH et al., 2021). On the other hand, the intermediate and lower values (Fig. 16) indicate the shift towards a closed or partially open system in which the sulphate content was limited, which leads to utilisation of heavier ^{34}S in microbial sulphate reduction, as the sulphate with ^{32}S was depleted and not replenished (CHAMBERS & TRUDINGER, 1979; ALGEO et al., 2015; HOUGH et al., 2019; PASQUIER et al., 2021). This was also observed in other studies (ZARASVANDI et al., 2012; ELLAHI et al., 2015; ZHAO et al., 2023), and in the case of the Minjera bauxites it can be related to their progressive and final burial, which led to the hydrological closure of this system. The progressive closure could also be related to the progressive undersaturation of pore solutions with respect to pyrite, as indicated by the presence of euhedral, dendritic and acicular pyrite in the later stages (Figs. 8E–H, 17 and 17C), as the sulphur content became a limiting factor during its precipitation.

6.3. Geochemistry of the Minjera bauxites

When comparing the trace element composition of the Minjera bauxites with the Upper Continental Crust values (TAYLOR & MCLENNAN, 1985), they are enriched in most trace elements such as lithophile and high field strength elements (HFSE), while being depleted in large ion lithophile elements (LILE, Fig. 13). This is commonly observed in most bauxite deposits as elements such as HFSE are retained during bauxitisation (MONGELLI, 1997; CALAGARI & ABEDINI, 2007; ABEDINI & CALAGARI, 2014; MONGELLI et al., 2014, ELLAHI et al., 2017; ABEDINI et al., 2020) while the more mobile elements including bases and LILE are leached away (MONGELLI, 1997; CALAGARI & ABEDINI, 2007; XIAO et al., 2021). Fractionation of trace elements changed

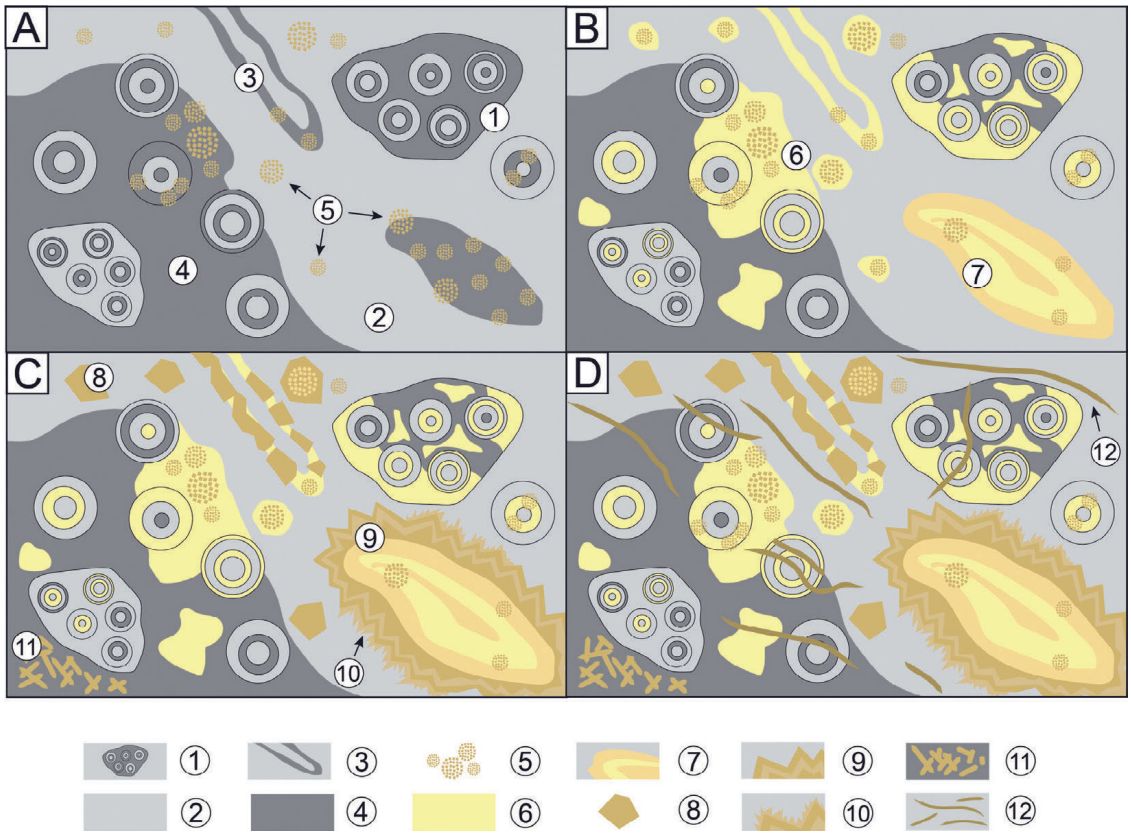

Figure 18. A schematic reconstruction of the succession of different iron sulphide morphologies. A – Formation of MSAP in the bauxite matrix (1), bauxite clasts (2), root remains (3) and ooid lamellae, coupled with the formation of pyrite framboids (4) together with MSAP or individually in the bauxite matrix; B – Overgrowth of colloform pyrite (6) over MSAP and framboids in the matrix, bauxite clasts, pyritised roots or ooid lamellae, which locally display banded textures (7); C – overgrowth and recrystallisation of framboids (8), MSAP and colloform pyrite into euhedral pyrite (9), followed by its overgrowth with dendritic pyrite (10) and formation of acicular pyrite in the matrix (11); D – formation of pyrite and kaolinite veins (12), over the previously formed iron sulphide morphologies and bauxite. Legend: 1 – MSAP; 2 – bauxite clasts; 3 – pyritised root remains; 4 – pyrite framboids; 5 – bauxite matrix; 6 – colloform pyrite; 7 – banded colloform pyrite; 8 – replacement of individual framboids with euhedral pyrite crystals; 9 – euhedral pyrite overgrowths; 10 – dendritic pyrite overgrowths; 11 – acicular pyrite; 12 – kaolinite and pyrite veins.

during the reduction and pyritisation of the red bauxite, as the newly established reducing and hydrogen sulphide-rich environment led to the accumulation and enrichment of chalcophile and redox-sensitive elements such as Cd, Hg, Mo, Se, and Tl (Fig. 13). This also affected the content of trace elements such as Pb and V which are preferentially enriched by iron oxides (WANTY & GOLDHABER, 1992; TABELIN et al., 2018; SHAHEEN et al., 2019), released during their reduction and dissolution, leading to their depletion in the pyritised bauxites compared to the red bauxite (Fig. 13). REEs were also affected by this process, since there is a significant depletion in MREEs within the pyritised bauxites (Fig. 14B, C), which is linked to the dissolution of iron oxides during their reduction which usually enriched the MREEs (TANG & JOHANNESSON, 2003; GRYBOS et al., 2007; LAVEUF et al., 2008; DAVRANCHE et al., 2011; ZHOU et al., 2020). This is further supported by the higher MREE content of the red bauxite sample compared to the pyritised bauxites (Fig. 15), confirming that they were indeed leached during the dissolution of iron oxides. Organic acids also preferentially adsorb MREEs compared to other REEs (GRYBOS et al., 2007; POURRET et al., 2007; DAVRANCHE et al., 2011), which could have been the mechanism through which they were removed from the bauxite as the organic-rich marshy environment was established on top of the bauxite. This is more pronounced in the organic-matter rich D15-6 sample, where LREEs and MREEs are even more depleted (Figs. 14C and 15). They also exhibit an enrichment in Hg, Mo, and Sb, which can be linked to the higher organic matter content of this sample (Figs. 13 and 14A). The pyritised bauxites also differ from red bauxite with respect to the Ce anomaly, as the red bauxite displays a negative Ce anomaly which is either weaker or absent in the pyritised bauxites (Figs. 14B–C and 14). The Ce anomaly in the red bauxite is likely a result of preferential retention of Ce in the upper parts of the bauxite (MONGELLI, 1997; WANG et al., 2013; VIND et al., 2018), since this leads to the development of a negative Ce anomaly in the lower sections of bauxites (MONGELLI, 1997). This negative anomaly could have been masked by the remobilisation of Ce in the presence of organic matter and acids during the flooding of the bauxite. This process preferentially concentrated Ce (POURRET et al., 2008; DAVRANCHE et al., 2011), because this could have caused its redistribution in the pyritised bauxite, masking the previously developed Ce anomalies.

The trace elemental content also supports the differences between the D-1 and D-15 deposits discussed in section 6.1, as besides the aforementioned differences in major elements between the deposits, the D-15 deposit also displays higher values of leachable elements such as Ca, K, Mg, Mn and LILE compared to D-1 (Figs. 12 and 13), which is in turn enriched in chalcophile elements such as As, Cu, Co, Ni and Sb (Fig. 13), indicating their association with iron sulphides which are much more abundant in the D-1 deposit. The higher Y/Ho ratio in the D-1 deposit compared to the D-15 deposit (Fig. 15) also indicates its higher degree of leaching, as this ratio can be used as a proxy for the intensity of water–rock interactions in soils (JI et al., 2004; FENG, 2010), since Ho is more mobile than Y in the aqueous environment (BAU et al., 1997; DIAKONOV et al., 1998) and complexes more easily with organic matter and HCO_3^- (KAWABE et al., 1991). The higher content of leachable elements in the D-15 deposit is also related to the greater alkalinity in this deposit, indicated by the higher La/Y values compared to the D-1 deposit (Fig. 15), which are commonly used as pH proxies in bauxites, with values >1 indicating formation under alkaline conditions (MAKSIMOVIĆ & PANTÓ, 1991). The increased alkalinity is also evident from the higher total REE content in the D-15 deposit (Fig. 15), as REEs are more stable in alkaline solutions (CAO et al., 2001; FERREIRA DA SILVA et al., 2009; OLÍAS et al., 2018).

6.4. Bauxite cover sequence

The Palaeocene lacustrine limestone cover sequence began with coal intercalations overlying the dark brown bauxite rich in organic matter, altogether indicating the flooding of a previously exposed karst terrain. The topmost section of the bauxite is commonly intermixed with carbonate clasts and boulders (Fig. 6A, B), which were likely eroded from the surrounding carbonate rocks and embedded within the bauxites during the initial flooding. The first part of the cover sequence was deposited in a lacustrine environment with typical flora and fauna composed of fresh water green algae *Cladophorites*, ostracods, gastropods and Charophyta. The strengthening of a marine influence is visible upwards in the cover sequence through the common presence of benthic foraminifera. This phase is linked to the internal transgression of the exposed carbonate terrain, which was later followed by overland transgression, during which the fully marine Foraminiferal limestones were deposited. The evolution of the bauxite cover from restricted lacustrine, brackish and freshwater environments towards fully marine carbonate deposition can be described as a typical "blue hole" sequence (RASMUSSEN & NEUMANN, 1988, CARANNANTE et al., 1994a, b). The presence of coal-seams, organic matter and plant remains in the top sections of the bauxite and the rest of the cover sequence confirms the establishment of a marshy environment on top of the bauxites, which served as a source of organic matter for microbial sulphate reduction.

7. CONCLUSIONS

This study focused on the genesis of the historically important Minjera bauxites, situated in the western part of the Savudrija–Buzet anticline, which developed during the subaerial exposure phase that marked the end of the Cretaceous and Palaeocene periods in Istria. This was done using the trace and rare earth elements as proxies for the physicochemical changes during the formation of the studied bauxites, as well as stable sulphur isotopes and iron sulphide morphology. This study also focused on the evolution of the cover in the studied bauxite deposits, in order to reconstruct the immediate palaeoenvironmental changes that followed the subaerial exposure phase. Several conclusions can be drawn from the collected data and their interpretation:

1 – The parent material from which the Minjera bauxites developed was polygenetic in origin, and was accumulated and bauxitised in karstic canyons and sinkholes developed over upper Cenomanian limestones the shallowing trend

of which and subaerial exposure features anticipated the long-lasting subaerial exposure phase during which the Istrian Palaeogene bauxites developed.

2 – The pyritisation of the Minjera bauxites produced geochemical differences between the originally red bauxite and the pyritised bauxite, as chalcophile elements were enriched during pyritisation under euxinic conditions, while the MREEs, V, and Pb were dissolved and depleted as a consequence of the solubilisation of iron oxides.

3 – Petrographic, mineralogical and geochemical differences were observed between the D-1 and D-15 deposits, as the D-1 deposit contains more pyrite, boehmite, chalcophile elements and a higher Y/Ho ratio, while the D-15 deposit formed in more alkaline conditions, and contains more kaolinite as well as more leachable elements such as LILE, Mn, Ca, Mg and K. Based on this, the D-1 deposit is of the true vadose type, which formed in a higher palaeotopographical position and higher above the water table compared to the D-15 deposit, which exhibits some features of phreatic bauxites and was formed in a lower palaeotopographic position, closer to the water table.

4 – Pyritisation in the Minjera bauxites was a multi-stage process. In the first phase, micrometre-sized anhedral pyrite and pyrite framboids were formed, which were later overgrown and replaced by colloform pyrite in the second phase, where all of these morphologies indicate that the solutions were supersaturated with respect to pyrite. In the following stages, euhedral, dendritic, and acicular pyrite formed, indicating that the solutions became undersaturated with respect to pyrite. The final stage of pyritisation is marked by the formation of pyrite veins.

5 – Stable sulphur isotopes support the diagenetic evolution of the system outlined by pyrite morphologies, as the $\delta^{34}S$ values exhibit a large range between -40.86 and 2.32 ‰. This indicates the evolution from an open system, during which the sulphate source was not restricted and the solutions were supersaturated with respect to pyrite, towards a closed system as the bauxite deposit was being progressively buried and more isolated, in which the sulphate supply was limited, leading to the drop in saturation of the solutions with respect to pyrite.

6 – The cover sequence of the bauxite is of Palaeocene age and can be described as a "blue hole" sequence, typical for the internal transgression of karst terrains, as it exhibits the transition from lacustrine conditions, characterised by fresh water green algae, charophyta and ostracods, towards a more marine environment indicated by the appearance of benthic foraminifera, before transitioning into the fully marine Foraminiferal limestones.

Based on the above, this study significantly added to the previous knowledge of the historically important Minjera bauxites, as it provides novel insight into their genesis and subsequent pyritisation. The detailed reconstruction of the different stages of their subsequent pyritisation is also a valuable addition to the current knowledge on pyritisation in bauxites, as few studies distinguished and described the pyritisation of a bauxite deposit in such detail. This study also revealed that the local differences in palaeorelief on subaerially exposed karst terrains can produce bauxites of different morphology and mineralogy, as well as different geochemical signatures. The important contribution is also the determination of the cover of Minjera deposits as Palaeocene, which is a new finding in the studied area.

ACKNOWLEDGEMENT

This work has been fully supported by the Croatian Science Foundation under the project IP-2019-04-8054 – WIANLab (Western Istrian Anticline as an Ideal Natural Laboratory for the Study of the Regional Unconformities in Carbonate Rocks; PI Professor Goran DURN).

REFERENCES

ABEDINI, A., AZIZI, M.R. & CALAGARI, A.A. (2019): Ree mobility and tetrad effects in bauxites: An example from the Kanisheeteh deposit, NW Iran.– Acta Geodynamica et Geomaterialia, 16/1, 11–26. doi: 10.13168/AGG.2019.0002

ABEDINI, A. & CALAGARI, A.A. (2014): REE geochemical characteristics of titanium-rich bauxites: The Permian Kanigorgeh horizon, NW Iran.– Turkish Journal of Earth Sciences, 23, 513–532. doi: 10.3906/yer-1404-11

ABEDINI, A., CALAGARI, A.A. & AZIZI, M.R. (2018). The tetrad-effect in rare earth elements distribution patterns of titanium-rich bauxites: Evidence from the Kanigorgeh deposit, NW Iran.– Journal of Geochemical Exploration, 186, 129–142. doi: 0.1016/j.gexplo.2017.12.007

ABEDINI, A., MONGELLI, G., KHOSRAVI, M. & SINISI, R. (2020): Geochemistry and secular trends in the middle–late Permian karst bauxite deposits, northwestern Iran.– Ore Geology Reviews, 124, 1–20. doi: 10.1016/j.oregeorev.2020.103660

ALEVA, G.J.J. (1994): Laterites: Concepts, Geology, Morphology and Chemistry.– In: International Soil Reference and Information Center (ISRIC) The Corlat Handbook, Corlat Technical, ISRIC, Wageningen, 169 p.

ALGEO, T.J., LUO, G.M., SONG, H.Y., LYONS, T.W. & CANFIELD, D.E. (2015): Reconstruction of secular variation in seawater sulfate concentrations.– Biogeosciences, 12/7, 2131–2151. doi: 10.5194/bg-12-2131-2015

BÁRDOSSY, G. (1982): Karst Bauxites: Bauxite Deposits on Carbonate Rocks.– Elsevier Scientific Publishing Company, Amsterdam–Oxford–New York, 441 p.

BARRIE, C.D., BOYCE, A.J., BOYLE, A.P., WILLIAMS, P.J., BLAKE, K., OGAWARA, T., AKAI, J. & PRIOR, D.J. (2009): Growth controls in colloform pyrite.– American Mineralogist, 94/4, 415–429. doi: 10.2138/am.2009.3053

BAU, M., MÖLLER, P. & DULSKI, P. (1997): Yttrium and lanthanides in eastern Mediterranean seawater and their fractionation during redox-cycling.– Marine Chemistry, 56/1–2, 123–131. doi: 10.1016/S0304-4203(96)00091-6

BERGANT, S., MATIČEC, D., FUČEK, L., PALENIK, D., KORBAR, T., ŠPARICA, M., KOCH, G., GALOVIĆ, I. & PRTOLJAN, B. (2020): Basic Geological Map of the Republic of Croatia scale 1:50.000, sheet: Rovinj 2.– Department of Geology, Croatian Geological Survey, Zagreb.

BERNER, R.A. (1970): Sedimentary pyrite formation.– American Journal of Science, 28, 1–23. doi: 10.2475/ajs.268.1.1

BRLEK, M., GAYNOR, S.P., MONGELLI, G., BAULUZ, B., SINISI, R., BRČIĆ, V., PEYTCHEVA, I., et al. (2021): Karst bauxite formation during Miocene Climatic Optimum (central Dalmatia, Croatia): mineralogical, compositional and geochronological perspectives.– International Journal of Earth Sciences, 110/531. doi: 10.1007/s00531-021-02091-z

CALAGARI, A.A. & ABEDINI, A. (2007): Geochemical investigations on Permo-Triassic bauxite horizon at Kanisheeteh, east of Bukan, West-Azarbaidjan, Iran.– Journal of Geochemical Exploration, 94/1, 1–18. doi: 10.1016/j.gexplo.2007.04.003

CANFIELD, D.E., RAISWELL, R., WESTRICH, J.T., REAVES, C.M. & BERNER, R.A. (1986): The use of chromium reduction in the analysis of reduced inorganic sulfur in sediments and shales.– Chemical Geology, 54/1, 149–155. doi: 10.1016/0009-2541(86)90078-1

CAO, X., CHEN, Y., WANG, X., & DENG, X. (2001): Effects of redox potential and pH value on the release of rare earth elements from soil.– Chemosphere, 44/4, 655–661. doi: 10.1016/S0045-6535(00)00492-6

CARANNANTE, G., MINDSZENTY, A., NEUMANN, A.C., RASMUSSEN, K.A., SIMONE, L. & TÓTH, K. (1994): Inland blue-hole-type ponds in the Mesozoic–Tertiary karst filling sequences.– In: IAS 15th Regional Meeting, Abstracts. Ischia, 102–103.

CARANNANTE, G., D'ARGENIO, B., MINDSZENTY, A., RUBERTI, D., & SIMONE, L. (1994). Cretaceous–Miocene shallow water carbonate sequences. Regional unconformities and facies patterns.– In: CARANNANTE, G & TONIELLI, R. (eds.): Field Trip Guide Book: 15th Regional IAS Meeting. De Frede, Napoli, 25–60.

CAVALAZZI, B., BARBIERI, R., CADY, S.L., GEORGE, A.D., GENNARO, S., WESTALL, F., LUI, A., et al. (2012): Iron-framboids in the hydrocarbon-related Middle Devonian Hollard Mound of the Anti-Atlas mountain range in Morocco: Evidence of potential microbial biosignatures.– Sedimentary Geology, 263/264,183–264. doi: 10.1016/j.sedgeo.2011.09.007

CHAMBERS, L.A. & TRUDINGER, P.A. (1979): Microbiological fractionation of stable sulfur isotopes: a review and critique.– Geomicrobiology Journal, 1/3, 249–293. doi: 10.1080/01490457909377735

CHEN, J., WANG, Q., ZHANG, Q., CARRANZA, E.J.M. & WANG, J. (2018): Mineralogical and geochemical investigations on the iron-rich gibbsitic bauxite in Yongjiang basin, SW China.– Journal of Geochemical Exploration, 188. doi: 10.1016/j.gexplo.2018.02.007

CHEN, P., LIU, B., WANG, T., ZHOU, L., WANG, Y., SUN, G., HOU, K., et al. (2022): Genesis of the Danping bauxite deposit in northern Guizhou, Southwest China: Constraints from in-situ elemental and sulfur isotope analyses in pyrite.– Ore Geology Reviews, 148. doi: 10.1016/j.oregeorev.2022.105056

CHEN, T. (1978): Colloform and framboidal pyrite from the Caribou deposit, New Brunswick.– Canadian Mineral., 16/1, 9–15.

D'AMBROSI, C. (1926): Rapporti fra morfologia e trasgresioni nel Cretaceo e nel terziario dell'Istria.– Atti Della Accademia Scientifica Veneto–Trentino–Istriana, 16/13, 90–98.

D'ARGENIO, B. & MINDSZENTY, A. (1995): Bauxites and related paleokarst: tectonic and climatic event markers at regional unconformities.– Eclogae Geologicae Helvetiae, 88/3, 453–499.

DAVRANCHE, M., GRYBOS, M., GRUAU, G., PÉDROT, M., DIA, A. & MARSAC, R. (2011): Rare earth element patterns: A tool for identifying trace metal sources during wetland soil reduction.– Chemical Geology, 284/1–2, 127–137. doi: 10.1016/j.chemgeo.2011.02.014

DIAKONOV, I.I., RAGNARSDOTTIR, K.V. & TAGIROV, B.R. (1998): Standard thermodynamic properties and heat capacity equations of rare earth hydroxides: II. Ce(III)-, Pr-, Sm-, Eu(III)-, Gd-, Tb-, Dy-, Ho-, Er-, Tm-, Yb-, and Y-hydroxides. Comparison of thermochemical and solubility data.– Chemical Geology, 151/1–4, 327–347. doi: 10.1016/s0009-2541(98)00088-6

DOEBELIN, N. & KLEEBERG, R. (2015): Profex: A graphical user interface for the Rietveld refinement program BGMN.– Journal of Applied Crystallography, 48, 1573–1580. doi: 10.1107/S1600576715014685

DRAGOVIĆ, D. (1989): The red and white karstic bauxites of Montenegro (Yugoslavia.).– Travaux, 19/22, 249–257.

DURN, G., MINDSZENTY, A., TIŠLJAR, J. & MILEUSNIĆ, M. (2006): Clay mineralogy of bauxites and palaeosols in Istria formed during regional subaerial exposures of the Adriatic Carbonate Platform.– In: VLAHOVIĆ, I., TIBLJAŠ, D. & DURN, G. (eds.): 3rd Mid-European Clay Conference: Field Trip Guidebook, University of Zagreb, Faculty of Science and Faculty of Mining, Geology and Petroleum Engineering, Zagreb, Croatia, 3–30.

DURN, G., OTTNER, F., TIŠLJAR, J., MINDSZENTY, A. & BARUDŽIJA, U. (2003): Regional subaerial unconformities in shallow-marine carbonate sequences of Istria: Sedimentology, mineralogy, geochemistry and micromorphology of associated bauxites, palaeosols and pedo-sedimentary complexes.– In VLAHOVIĆ, I. & TIŠLJAR, J. (eds.): Field Trip Guidebook: Evolution of Depositional Environments from the Palaeozoic to the Quaternary in the Karst Dinarides and the Pannonian Basin. 22nd IAS Meeting of Sedimentology, Institute of Geology Zagreb, Zagreb, 209–255.

DURN, G., PERKOVIĆ, I., MILEUSNIĆ, M., VLAHOVIĆ, I., RUŽIČIĆ, S., MATEŠIĆ, D., CVETKO TEŠOVIĆ, B., et al. (2023): Red Istria: Western Istrian Anticline as an ideal natural laboratory for the study of the regional unconformities in carbonate rocks.– In: FIO FIRI, K. & ČOBIĆ, A. (eds.): Field trip A2, Excursion Guide-Book, 7th Croatian Geological Congress with International Participation, Hrvatski geološki institut, Zagreb, 33–58.

ECONOMOU-ELIOPOULOS, M., KONTOU, M. & MEGREMI, I. (2022): Biogeochemical redox processes controlling the element cycling: Insights from karst-type bauxite, Greece.– Minerals, 12/4:446. doi: 10.3390/min12040446

ELLAHI, S.S., TAGHIPOUR, B. & NEJADHADAD, M. (2017): The role of organic matter in the formation of high-grade Al deposits of the Dopolan karst type bauxite, Iran: Mineralogy, geochemistry, and sulfur isotope data.– Minerals, 7/6. doi: 10.3390/min7060097

ELLAHI, S.S., TAGHIPOUR, B., ZARASVANDI, A., BIRD, M.I. & D SOMARIN, A.K. (2015): Mineralogy, geochemistry and stable isotope studies of the Dopolan bauxite deposit, Zagros mountain, Iran.– Minerals, 6/1. doi: 10.3390/min6010011

FENG, J. L. (2010): Behaviour of rare earth elements and yttrium in ferromanganese concretions, gibbsite spots, and the surrounding terra rossa over dolomite during chemical weathering.– Chemical Geology, 271/3–4, 112–132. doi: 10.1016/j.chemgeo.2010.01.003

FERREIRA DA SILVA, E., BOBOS, I., XAVIER MATOS, J., PATINHA, C., REIS, A.P. & CARDOSO FONSECA, E. (2009): Mineralogy and geochemistry of trace metals and REE in volcanic massive sulfide host rocks, stream sediments, stream waters and acid mine drainage from the Lousal mine area (Iberian Pyrite Belt, Portugal).– Applied Geochemistry, 24/3, 383–401. doi: 10.1016/j.apgeochem.2008.12.001

FLÜGEL, E. (2004): Microfacies of Carbonate Rocks, Microfacies of Carbonate Rocks.– Springer Verlag, Berlin, 976 p. doi: 10.1007/978-3-662-08726-8

GAMALETSOS, P.N., GODELITSAS, A., KASAMA, T., CHURCH, N.S., DOUVALIS, A.P., GÖTTLICHER, J., STEININGER, R., et al. (2017): Nano-mineralogy and geochemistry of high-grade diasporic karst-type bauxite from Parnassos–Ghiona mines, Greece.– Ore Geology Reviews, 84. doi: 10.1016/j.oregeorev.2016.11.009

GRAULIS, S., CHATEIGNER, D., DOWNS, R.T., YOKOCHI, A.F.T., QUIRÓS, M., LUTTEROTTI, L., MANAKOVA, E., et al. (2009): Crystallography Open Database – An open-access collection of crystal structures.– Journal of Applied Crystallography, 42/4. doi: 10.1107/S0021889809016690

GRYBOS, M., DAVRANCHE, M., GRUAU, G. & PETITJEAN, P. (2007): Is trace metal release in wetland soils controlled by organic matter mobility or Fe-oxyhydroxides reduction?– Journal of Colloid and Interface Science, 314/2, 490–501. doi: 10.1016/j.jcis.2007.04.062

HÁMOR, T. (1994): The occurrence and morphology of sedimentary pyrite.– Bulletin of the Hungarian Geological Society, 37/1–2, 153–181.

HE, J., YANG, L., SHI, X., ZHAO, S., CAO, L., PAN, S., WU, F., et al. (2022): Genetic Mechanism of Pyrite in the Shale of the Longmaxi Formation and Its Influence on the Pore Structure: A Case Study of the Changning Area, South Sichuan Basin of SW China.– Frontiers in Earth Science, 10. doi: 10.3389/feart.2022.919923

VAN HINSBERGEN, D.J.J., TORSVIK, T.H., SCHMID, S.M., MAŢENCO, L.C., MAFFIONE, M., VISSERS, R.L.M., GÜRER, D., et al. (2020): Orogenic architecture of the Mediterranean region and kinematic reconstruction of its tectonic evolution since the Triassic.– Gondwana Research, 81, 79–229. doi. 10.1016/j.gr.2019.07.009

HOUGH, G., SWAPP, S., FROST, C. & FAYEK, M. (2019): Sulfur isotopes in biogenically and abiogenically derived uranium roll-front deposits.– Economic Geology, 114/2, doi: 10.5382/econgeo.2019.4634

HUANG, F., GAO, S., CHEN, L., SU, L., LI, Y., MENG, L., LIU, K., et al. (2020): Micro-texture and in situ sulfur isotope of pyrite from the Baiyunpu Pb–Zn deposit in central Hunan, South China: Implications for the growth mechanism of colloform pyrite aggregates.– Journal of Asian Earth Sciences, 193. doi: 10.1016/j.jseaes.2020.104302

JEŽ, J., OTONIČAR, B. (2018): Late Cretaceous geodynamics of the northern sector of the Adriatic Carbonate Platform (Western Slovenia).– Newsletters on Stratigraphy, 51/4, 381–410.

JI, H., WANG, S., OUYANG, Z., ZHANG, S., SUN, C., LIU, X. & ZHOU, D. (2004): Geochemistry of red residua underlying dolomites in karst terrains of Yunnan–Guizhou Plateau II. The mobility of rare earth elements during weathering.– Chemical Geology, 203/1–2, 1–27. doi: 10.1016/j.chemgeo.2003.08.012

KAWABE, I., KITAHARA, Y. & NAITO, K. (1991): Non-chondritic yttrium/holmium ratio and lanthanide tetrad effect observed in pre-Cenozoic limestones.– Geochemical Journal, 25/1, 31–44. doi:10.2343/geochemj.25.31

KELEMEN, P., DUNKL, I., CSILLAG, G., MINDSZENTY, A., VON EYNATTEN, H. & JÓZSA, S. (2017): Tracing multiple resedimentation on an isolated karstified plateau: The bauxite-bearing Miocene red clay of the Southern Bakony Mountains, Hungary.– Sedimentary Geology, 358/1, 84–96. doi: 10.1016/j.sedgeo.2017.07.005

KELEMEN, P., DUNKL, I., CSILLAG, G., MINDSZENTY, A., JÓZSA, S., FODOR, L. & VON EYNATTEN, H. (2023): Origin, timing and paleogeographic implications of Paleogene karst bauxites in the northern Transdanubian range, Hungary.– International Journal of Earth Sciences, 112/1. doi: 10.1007/s00531-022-02249-3

LASKOU, M. & ECONOMOU-ELIOPOULOS, M. (2007): The role of microorganisms on the mineralogical and geochemical characteristics of the Parnassos–Ghiona bauxite deposits, Greece.– Journal of Geochemical Exploration, 93/2, 67–77. doi: 10.1016/j.gexplo.2006.08.014

LASKOU, M. & ECONOMOU-ELIOPOULOS, M. (2013): Bio-mineralization and potential biogeochemical processes in bauxite deposits: Genetic and ore quality significance.– Mineralogy and Petrology, 107/4, 471–486. doi: 10.1007/s00710-012-0257-z

LAVEUF, C., CORNU, S. & JUILLOT, F. (2008): Rare earth elements as tracers of pedogenetic processes.– Comptes Rendus – Geoscience, 340/8, 523–532. doi: 10.1016/j.crte.2008.07.001

LIU, X., WANG, Q., FENG, Y., LI, Z. & CAI, S. (2013). Genesis of the Guangou karstic bauxite deposit in western Henan, China.– Ore Geology Reviews, 55/C, 162–175. doi: 10.1016/j.oregeorev.2013.06.002

MAKSIMOVIĆ, Z., MINDSZENTY, A. & PANTO, G. (1991): Contribution to the geochemistry of Hungarian karst bauxites and the allochthony/autochthony problem.– Acta Geologica Hungarica, 34/4, 317–334.

MAKSIMOVIĆ, Z. & PANTÓ, G. (1991): Contribution to the geochemistry of the rare earth elements in the karst-bauxite deposits of Yugoslavia and Greece.– Geoderma, 51/1–4, 93–109. doi: 10.1016/0016-7061(91)90067-4

MAMELI, P., MONGELLI, G., OGGIANO, G. & DINELLI, E. (2007): Geological, geochemical and mineralogical features of some bauxite deposits from Nurra (Western Sardinia, Italy) Insights on conditions of formation and parental affinity.– International Journal of Earth Sciences, 96/5, 887–902. doi:10.1007/s00531-006-0142-2

MATIČEC, D., VLAHOVIĆ, I., VELIĆ, I. & TIŠLJAR, J. (1996): Eocene limestones overlying Lower Cretaceous deposits of western Istria (Croatia): did some parts of present Istria form land during the Cretaceous.– Geologia Croatica, 49/1, 117–127. doi: 10.4154/GC.1994.46

MEDERSKI, S., PRŠEK, J., MAJZLAN, J., KIEFER, S., DIMITROVA, D., MILOVSKÝ, R., KOCH, C.B., et al. (2022): Geochemistry and textural evolution of As–Tl-Sb-Hg-rich pyrite from a sediment-hosted As-Sb-Tl-Pb ± Hg ± Au mineralization in Janjevo, Kosovo.– Ore Geology Reviews, 151, doi: 10.1016/j.oregeorev.2022.105221

MEHRA, O.P. & JACKSON, M.L. (1960), Iron Oxide Removal From Soils and Clays By a Dithionite–Citrate System Buffered With Sodium Bicarbonate.– In: Clays and clay minerals: Proceedings of the Seventh National Conference, Clays and Clay Minerals.

MO, H., YANG, R., LUO, C., LI, X., JI, Y., YANG, G., ZHOU, X., et al. (2023): Effect of Karst Geomorphology on the Sedimentary Mineralization and Geochemical Distribution of Bauxite: An Example from the Xiaoyuan Area in Qingzhen, Guizhou Province.– Minerals, 13/8. doi: 10.3390/min13081013

MONDILLO, N., DI NUZZO, M., KALAITZIDIS, S., BONI, M., SANTORO, L. & BALASSONE, G. (2022): Petrographic and geochemical features of the B3 bauxite horizon (Cenomanian–Turonian) in the Parnassos–Ghiona area: A contribution towards the genesis of the Greek karst bauxites.– Ore Geology Reviews, 143. doi: 10.1016/j.oregeorev.2022.104759

MONGELLI, G. (1997): Ce-anomalies in the textural components of Upper Cretaceous karst bauxites from the Apulian carbonate platform (southern Italy).– Chemical Geology, 140/1–2, 69–79. doi: 10.1016/S0009-2541(97)00042-9

MONGELLI, G., BONI, M., BUCCIONE, R. & SINISI, R. (2014): Geochemistry of the Apulian karst bauxites (southern Italy): Chemical fractionation and parental affinities.– Ore Geology Reviews, 63, 9–21. doi: 10.1016/j.oregeorev.2014.04.012

MONGELLI, G., BONI, M., OGGIANO, G., MAMELI, P., SINISI, R., BUCCIONE, R. & MONDILLO, N. (2017): Critical metals distribution in Tethyan karst bauxite: The cretaceous Italian ores.– Ore Geology Reviews, 86, 526–536. doi: 10.1016/j.oregeorev.2017.03.017

MONGELLI, G., MAMELI, P., SINISI, R., BUCCIONE, R. & OGGIANO, G. (2021): Rees and other critical raw materials in Cretaceous Mediterranean-type bauxite: The case of the Sardinian ore (Italy).– Ore Geology Reviews, 139/B. doi: 10.1016/j.oregeorev.2021.104559

NIA, R. (1968): Geologische, petrographische, geochemische Untersuchungen zum Problem der Boehmit-Diaspor-Genese in griechischen Oberkreide-Bauxiten der Parnass-Kiona-Zone.– PhD thesis, University of Hamburg, 1–133.

OTONIČAR, B. (2006): Upper Cretaceous to Palaeogene forebulge unconformity associated with foreland basin evolution (Kras, Matarsko polje and Istria, southwestern Slovenia and northwestern Croatia).– Acta Carsologica, 36/1, 101–120. doi.org/10.3986/ac.v36i.213

OLÍAS, M., CÁNOVAS, C.R., BASALLOTE, M.D. & LOZANO, A. (2018): Geochemical behaviour of rare earth elements (REE) along a river reach receiving inputs of acid mine drainage–. Chemical Geology, 493, 468–477. doi: 10.1016/j.chemgeo.2018.06.029

ÖZTÜRK, H., HEIN, J.R. & HANILÇI, N. (2002): Genesis of the Doğankuzu and Mortaş bauxite deposits, Taurides, Turkey: Separation of Al, Fe, and Mn and implications for passive margin metallogeny.– Economic Geology, 97/5, 1063–1077. doi: 10.2113/gsecongeo.97.5.1063

PASQUIER, V., FIKE, D.A. & HALEVY, I. (2021): Sedimentary pyrite sulfur isotopes track the local dynamics of the Peruvian oxygen minimum zone.– Nature Communications, 12/1:440312/1. doi: 10.1038/s41467-021-24753-x

POURRET, O., DAVRANCHE, M., GRUAU, G. & DIA, A. (2007): Rare earth elements complexation with humic acid.– Chemical Geology, 243/1–2, 128–141. doi: 10.1016/j.chemgeo.2007.05.018

POURRET, O., DAVRANCHE, M., GRUAU, G. & DIA, A. (2008): New insights into cerium anomalies in organic-rich alkaline waters.– Chemical Geology, 251/1–4, 120–127. doi: 10.1016/j.chemgeo.2008.03.002

RADUSINOVIĆ, S. & PAPADOPOULOS, A. (2021): The potential for REE and associated critical metals in karstic bauxites and bauxite residue of Montenegro.– Minerals, MDPI, 11/9, 975. doi: 10.3390/min11090975

RAISWELL, R. (1982): Pyrite texture, isotopic composition and the availability of iron.– American Journal of Science, 282/8, 1244–1263. doi: 10.2475/ajs.282.8.1244

RASMUSSEN, K., NEUMANN, A.C.N. (1988): Holocene overprint of Pleistocene paleokarst: Bight of Abaco, Bahamas.– In: JAMES, N.P., CHOQUETTE P.W. (eds.): Paleokarst. Springer-Verlag, 132–148.

ROEDDER, E. (1968): The non-colloidal origin of 'colloform' textures in sphalerite ores.– Economic Geology, 63/5, 451–471. doi: 10.2113/gsecongeo.63.5.451

SCHMID, S.M., BERNOULLI, D., FÜGENSCHUH, B., MATENCO, L., SCHEFER, S., SCHUSTER, R., TISCHLER, M., et al. (2008): The Alpine–Carpathian–Dinaridic orogenic system: Correlation and evolution of tectonic units.– Swiss Journal of Geosciences, 101/1, 139–183. doi: 10.1007/s00015-008-1247-3

SCHMID, S.M., FÜGENSCHUH, B., KOUNOV, A., MAŢENCO, L., NIEVERGELT, P., OBERHÄNSLI, R., PLEUGER, J., et al. (2020): Tectonic units of the Alpine collision zone between Eastern Alps and western Turkey.– Gondwana Research, 308–374. doi: 10.1016/j.gr.2019.07.005

SHAHEEN, S.M., ALESSI, D.S., TACK, F.M.G., OK, Y.S., KIM, K.H., GUSTAFSSON, J.P., SPARKS, D.L., et al. (2019). Redox chemistry of vanadium in soils and sediments: Interactions with colloidal materials, mobilization, speciation, and relevant environmental implications – A review.– Advances in Colloid and Interface Science, 265, 1–13. doi: 10.1016/j.cis.2019.01.002

ŠINKOVEC, B., SAKAČ, K. & DURN, G. (1994): Pyritized bauxites from Minjera, Istria, Croatia.– Natura Croatica, 3/1, 41–65.

TABELIN, C.B., IGARASHI, T., VILLACORTE-TABELIN, M., PARK, I., OPISO, E.M., ITO, M. & HIROYOSHI, N. (2018): Arsenic, selenium, boron, lead, cadmium, copper, and zinc in naturally contaminated rocks: A review of their sources, modes of enrichment, mechanisms of release, and mitigation strategies.– Science of the Total Environment, 645/7, 1522–1553. doi: 10.1016/J.SCITOTENV.2018.07.103

TANG, J. & JOHANNESSON, K.H. (2003): Speciation of rare earth elements in natural terrestrial waters: Assessing the role of dissolved organic matter from the modeling approach.– Geochimica et Cosmochimica Acta, 67/13, 2321–2339. doi: 10.1016/S0016-7037(02)01413-8

TAYLOR, S.R. & MCLENNAN, S.M. (1985): The Continental Crust: Its Composition and Evolution, The Continental Crust: Its Composition and Evolution. An Examination of the Geochemical Record Preserved in Sedimentary Rocks.– Blackwell Science, Oxford, 312 p.

TOMAŠIĆ, N., ČOBIĆ, A., BEDEKOVIĆ, M., MIKO, S., ILIJANIĆ, N., GIZDAVEC, N. & MATOŠEVIĆ, M. (2021): Rare earth elements enrichment in the Upper Eocene Tošići-Dujići bauxite deposit, Croatia, and relation to ree mineralogy, parent material and weathering pattern.– Minerals, 11/1:1260. doi: 10.3390/min11111260

VELIĆ, I., MATIČEC, D., TIŠLJAR, J. & VLAHOVIĆ, I. (1995): Opći prikaz geološke građe Istre (A review of the geology of Istria).– In: VLAHOVIĆ, I. & VELIĆ, I. (eds.): 1st Croatian Geological Congress, Excursion Guidebook. Croatian Geological survey, Zagreb, 5–30.

VIND, J., MALFLIET, A., BLANPAIN, B., TSAKIRIDIS, P.E., TKACZYK, A.H., VASSILIADOU, V. & PANIAS, D. (2018): Rare earth element phases in bauxite residue.– Minerals, 8/2:77. doi: 10.3390/min8020077

VLAHOVIĆ, I., TIŠLJAR, J. & VELIĆ, I. (1994): Influence of synsedimentary tectonics and eustatic changes on deposition of the Cenomanian platform carbonates in Istria (Western Croatia).– Géologie Méditerranéenne, 21/3–4, 189–193. doi: 10.3406/geolm.1994.1561

VLAHOVIĆ, I., TIŠLJAR, J., VELIĆ, I. & MATIČEC, D. (2005): Evolution of the Adriatic Carbonate Platform: Palaeogeography, main events and depositional dynamics.– Palaeogeography, Palaeoclimatology, Palaeoecology, 220/3–4, 333–360. doi: 10.1016/j.palaeo.2005.01.011

WANG, X., JIAO, Y., DU, Y., LING, W., WU, L., CUI, T., ZHOU, Q., et al. (2013): REE mobility and Ce anomaly in bauxite deposit of WZD area, Northern Guizhou, China.– Journal of Geochemical Exploration, 133, 103–117. doi: 10.1016/j.gexplo.2013.08.009

WANG, B., LEI, H. & HUANG, F. (2022): Impacts of sulfate-driven anaerobic oxidation of methane on the morphology, sulfur isotope, and trace element content of authigenic pyrite in marine sediments of the northern South China Sea.– Marine and Petroleum Geology, 139. doi: 10.1016/j.marpetgeo.2022.105578

WANTY, R.B. & GOLDHABER, M.B. (1992): Thermodynamics and kinetics of reactions involving vanadium in natural systems: Accumulation of vanadium in sedimentary rocks.– Geochimica et Cosmochimica Acta, 56/4, 1471–1483. doi: 10.1016/0016-7037(92)90217-7

WIGNALL, P.B. & NEWTON, R. (1998): Pyrite framboid diameter as a measure of oxygen deficiency in ancient mudrocks.– American Journal of Science, 298/7, 537–552. doi: 10.2475/ajs.29

WILKIN, R.T., BARNES, H.L. (1996): Pyrite formation by reactions of iron monosulfides with dissolved inorganic and organic sulfur species.– Geochimica et Cosmochimicha.Acta, 60/21, 4167–4179. doi: 10.1016/S0016-7037(97)81466-4

WILLIAMS, J.R. (2014): Karst-Associated Bauxite Deposits of Parnassos–Ghiona, Central Greece: Ore Genesis and Structural Evolution.– Ph.D. Thesis, University of Brighton, 311 p.

XIAO, J., LI, Y., YANG, H., XU, J. & HUANG, M. (2021): Geochemistry of the Yudong bauxite deposit, south-eastern Guizhou, China: Implications for conditions of formation and parental affinity.– Journal of Geochemical Exploration, 220. doi: 10.1016/j.gexplo.2020.106676

YANG, L., WANG, Q., ZHANG, Q., CARRANZA, E.J.M., LIU, H., LIU, X. & DENG, J. (2017): Interaction between karst terrain and bauxites: Evidence from Quaternary orebody distribution in Guangxi, SW China.– Scientific Reports, 7/1. doi: 10.1038/s41598-017-12181-1

YANG, S., WANG, Q., DENG, J., WANG, Y., KANG, W., LIU, X. & LI, Z. (2019): Genesis of karst bauxite-bearing sequences in Baofeng, Henan (China), and the distribution of critical metals.– Ore Geology Reviews, 115. doi: 10.1016/j.oregeorev.2019.103161

YUE, L., JIAO, Y., WU, L., RONG, H., FAYEK, M. & XIE, H. (2020): Evolution and origins of pyrite in sandstone-type uranium deposits, northern Ordos Basin, north-central China, based on micromorphological and compositional analysis.– Ore Geology Reviews, 118. doi: 10.1016/j.oregeorev.2020.103334

YUSTE, A., BAULUZ, B. & MAYAYO, M.J. (2017): Origin and geochemical evolution from ferrallitized clays to karst bauxite: An example from the Lower Cretaceous of NE Spain.– Ore Geology Reviews, 84/3, 67–79. doi: 10.1016/j.oregeorev.2016.12.025

ZARASVANDI, A., CARRANZA, E.J.M. & ELLAHI, S.S. (2012): Geological, geochemical, and mineralogical characteristics of the Mandan and Deh-now bauxite deposits, Zagros Fold Belt, Iran.– Ore Geology Reviews, 48, 125–138. doi: 10.1016/j.oregeorev.2012.02.010

ZHANG, J.-Y., WANG, Q., LIU, X.-F., ZHOU, G.-F., XU, H.-P. & ZHU, Y.-G. (2022): Provenance and ore-forming process of Permian lithium-rich bauxite in central Yunnan, SW China.– Ore Geology Reviews, 145. doi: 10.1016/j.oregeorev.2022.104862

ZHAO, L., LIU, X., WANG, Q., MA, X., LIU, L., SUN, X. & DENG, J. (2023): Genetic mechanism of super-large karst bauxite in the northern North China Craton: Constrained by diaspore in-situ compositional analysis and pyrite sulfur isotopic compositions.– Chemical Geology, 622. doi: 10.1016/j.chemgeo.2023.121388

ZHOU, W., HAN, G., LIU, M., SONG, C. & LI, X. (2020): Geochemical distribution characteristics of rare earth elements in different soil profiles in Mun River Basin, Northeast Thailand.– Sustainability, 12/2, 457. doi: 10.3390/su12020457